Flow Intensification Due to the Superposition of Near-Inertial Internal Waves in the Abyssal Yamato and Tsushima Basins of the Japan Sea (East Sea)

千手, 智晴
Regional Oceanography Section, Division of Earth Environment Dynamics, Research Institute for Applied Mechanics, Kyushu University

Shin, Hong-Ryeol
Department of Atmospheric Sciences, Kongju National University

出版情報：Journal of Geophysical Research: Oceans. 126 (3), pp.e2020JC016647-, 2021-03-03. American Geophysical Union
バージョン：

JGR Oceans

RESEARCH ARTICLE
10.1029/2020JC016647

Flow Intensification Due to the Superposition of Near-Inertial Internal Waves in the Abyssal Yamato and Tsushima Basins of the Japan Sea (East Sea)

Tomoharu Senjyu[1] **and Hong-Ryeol Shin**[2]

[1]Regional Oceanography Section, Division of Earth Environment Dynamics, Research Institute for Applied Mechanics, Kyushu University, Kasuga, Japan, [2]Department of Atmospheric Sciences, Kongju National University, Gongju, Chungcheongnam-Do, Korea

Key Points:

- Near-inertial flow events with 3–5 days duration were observed in the abyssal Japan Sea using moored current meters
- Near-inertial flows during the events exhibited a vertically coherent phase and varying amplitude with depth
- Superposition of near-inertial internal waves was suggested as a cause of the deep flow intensification that promotes vertical mixing

Correspondence to:
T. Senjyu,
senjyu@riam.kyushu-u.ac.jp

Citation:
Senjyu, T., & Shin, H.-R. (2021). Flow intensification due to the superposition of near-inertial internal waves in the abyssal Yamato and Tsushima Basins of the Japan Sea (East Sea). *Journal of Geophysical Research: Oceans*, *126*, e2020JC016647. https://doi.org/10.1029/2020JC016647

Received 27 JUL 2020
Accepted 25 FEB 2021

Abstract Near-inertial internal waves (NIWs) in the abyssal Yamato and Tsushima Basins of the Japan Sea (East Sea) were investigated using data from a moored acoustic Doppler current profiler (ADCP) and single-point current meters. The NIW events with duration of 3–5 days were observed intermittently in both basins. In particular, an active NIW event occurred below 2,475 m in the Yamato Basin during May 12–16, 2014. This was followed by the upward propagation of a wave packet from 2,475 to 950 m. The near-inertial flows (1.07*f*) during the event exhibited a vertically coherent phase and intensification with depth by a factor of 1.5 from 2,475 to 2,635 m. The near-inertial flows (1.05*f*) in the Tsushima Basin also showed a vertically coherent phase and intensification with depth, although the amplitude of the flow exhibited a middepth maximum rather than monotonic intensification. As a possible explanation of the observed flow characteristics, the superposition of downward-propagating NIWs that can be excited by a strong wind event and upward-propagating NIWs that bounced off the seabed was examined. The time series of the Richardson number based on the observed shear showed sporadic unstable conditions during the initial stage of the NIW event during May 2014 in the Yamato Basin. In addition, relatively small values of Richardson number were observed over the range of 2,475–2,635 m during the period of active NIWs. This suggests the promotion of vertical mixing in the deep sea during significant NIW events.

Plain Language Summary The Japan Sea, a semi-closed marginal sea in East Asia, has its own circulation system driven by the deep water formation. We carried out deep flow observations in the sea 4 times using moored acoustic current meters. The current meters recorded strong flow events accompanying clockwise-rotating cyclic flows of 18–20 h periods. The cyclic flow, called the near-inertial flow, is associated with internal waves that are affected by the Earth rotation. The amplitude of near-inertial flow during the events varied vertically, although the direction of the flow was consistent throughout the observational depths. We tried to explain the observed flow intensification with depth by the superposition of downward-propagating internal wave that can be excited by a strong wind and upward-propagating internal wave that bounced off the seabed. In addition, we suggested that the intensification of near-inertial flow during the events promoted vertical mixing in the deep sea which controls pattern and strength of the deep circulation.

1. Introduction

Vertical mixing in the deep sea is essential for maintaining the global thermohaline circulation because cold, deep water originating from a high-latitude region acquires buoyancy via the vertical diffusion of heat from the upper layer during circulation. The main sources of energy for abyssal mixing are considered to be tides and wind (Munk & Wunsch, 1998). Active areas of vertical mixing have been reported in various regions worldwide, such as the Izu-Ogasawara and Hawaiian Ridges in the North Pacific (Niwa & Hibiya, 2001), and Mid-Atlantic Ridge of the Brazil Basin in the South Atlantic (Polzin et al., 1997). In these regions, interactions between tidal flows and bottom topography are known to be important. However, part of the wind energy is transmitted to the deep sea through near-inertial internal waves (NIWs). NIWs are thought to be important for water mass mixing in the interior of the oceans, because these waves dominate shear at most locations (Alford, MacKinnon, Pinkel, Klymak, 2017; Alford, MacKinnon, Simmons, & Nash, 2016). The

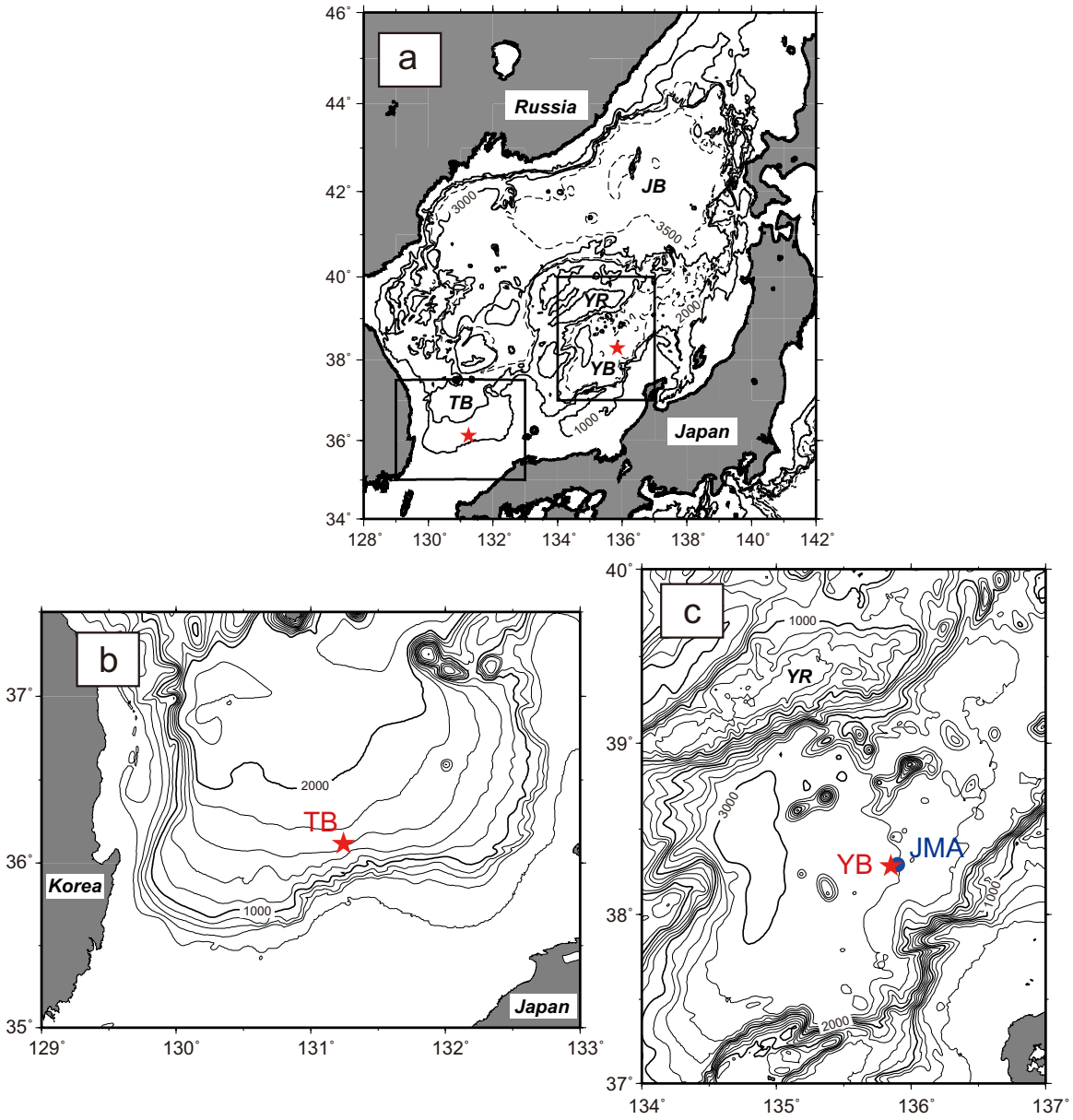

Figure 1. Bottom topography of (a) the Japan Sea, and (b and c) study areas. JB, YB, TB, and YR in (a) denote the Japan Basin, Yamato Basin, Tsushima Basin, and Yamato Rise, respectively. The red stars indicate the locations of the observation stations. The study areas indicated by the boxes in (a) are enlarged in (b) and (c). Sta. TB is indicated by a red star in (b). In (c), the red star and blue circles indicate Sta. YB and hydrographic stations of the Japan Meteorological Agency, respectively.

maps of the wind work on inertial motions exhibit midlatitude maxima with seasonal variations reflecting the travelling winter storms (Alford, 2001, 2003b; Watanabe & Hibiya, 2002).

The relative importance of tides and wind to the abyssal mixing is comparable from a global perspective (Munk & Wunsch, 1998). However, the wind contribution is likely to be more in a semi-enclosed sea where tidal activity is generally weak (Jordi & Wang, 2008; Puig et al., 2000; van der Lee & Umlauf, 2011). In fact, in the Japan Sea (East Sea) that is a semi-enclosed marginal sea in East Asia (Figure 1), tidal flows are negligible except in the Tsushima Basin in the southwest, although NIW signals can be observed throughout the Japan Sea (Senjyu, Shin, et al., 2005). In addition, the Japan Sea has its own thermohaline circulation system. The surface water that sinks into the deep layer of the northwestern region in winter circulates cyclonically in the abyssal regions of the Japan Sea (Senjyu, 2020; Senjyu, Aramaki, et al, 2002; Senjyu, Shin,

et al., 2005; Senjyu & Sudo, 1993, 1994). Therefore, the Japan sea provides an ideal natural laboratory to investigate the relationship between abyssal mixing, NIWs, and thermohaline circulation.

The near-inertial motions attributed to NIWs have frequently been reported in the abyssal Japan Sea (Park & Watts, 2005; Senjyu, Shin, et al., 2005; Takematsu et al., 1999). Mori et al. (2005) analyzed the historical current meter records obtained from 24 mooring stations in the entire area of the Japan Sea and revealed that significant NIWs with high energies are primarily observed in two southern basins: The Yamato and Tsushima Basins (Figure 1). The energy level in the inertial band generally increases in winter in accordance with the strong monsoonal winds over the sea, similar to other oceans (Alford, Cronin, & Klymak, 2012; Alford & Whitmont, 2007; Silverthorne & Toole, 2009). The snapshot observations using the lowered and shipboard acoustic Doppler current profilers (ADCPs) captured the overall features of the vertical propagation of NIWs (Shcherbina et al., 2003). Wave polarization based on the rotary spectral analysis showed a prevailing downward-propagating energy flux in the upper 500 m, whereas the net upward-propagating energy flux was observed at depths between 500 and 2,500 m. However, for the deep sea in particular, there is insufficient information regarding structure and behavior of NIWs owing to a lack of observations with sufficiently high spatial and temporal resolutions (Alford, 2010; Silverthorne & Toole, 2009; Tool, 2007).

Many numerical models have attempted to reproduce deep circulation in the Japan Sea (e.g., Hogan & Hurlburt, 2000; Kim, 2007; Park et al., 2013). However, most models have failed to reproduce a realistic deep flow field with a mean flow of a few centimeters per second, that is, the modeled deep flows tend to be substantially weaker than the observed flows. Uncertainty regarding the vertical diffusivity is one of the reasons for the discrepancy because most numerical models are sensitive to the magnitude and distribution of vertical diffusivity (Melet et al., 2013; Samelson, 1998). Therefore, understanding the structure and behavior of NIWs in the deep sea through observations is essential not only for the further improvement of model studies, but also for a better understanding of the dynamics of the thermohaline circulation system.

Senjyu (2015) carried out a preliminary observation of NIWs in the deep layer of the Yamato Basin in May 2013 using a moored ADCP set with a very short measurement interval (10 s). Although a clear signal of NIWs was captured successfully, a detailed analysis of the structure and behavior of NIWs was not possible owing to the short observation period (2 days). In this study, we report near-inertial flows with a vertically coherent phase but varying amplitude with depth obtained in more extensive observations undertaken in the Yamato and Tsushima Basins in the southern Japan Sea and try to explain the observed deep flow characteristics by the superposition of vertically propagating NIWs. The reflection of internal waves off a sloping bottom and consequent flow intensification have been studied theoretically and observationally (e.g., Eriksen, 1982; Phillips, 1977; Sarkar & Scotti, 2017). However, our study is based on the idea that NIWs generated in a wide area could interfere between incident and reflected waves even on a flat bottom. The contribution of the intensified flow to the deep mixing will also be discussed.

The remainder of this paper is organized as follows. In Section 2, our mooring observations and other data used in this study are described. The general descriptions of the flows observed in the Yamato and Tsushima Basins are presented in Section 3. The structure and propagation of significant NIWs observed in the Yamato Basin are discussed in Section 4 based on the band-pass filtered flow data. In Section 5, spatiotemporal characteristics of the near-inertial flows observed in both basins are examined focusing on their phase and amplitude. As a possible explanation of the observed flow characteristics, the superposition of upward- and downward-propagating NIWs is discussed in Section 6. Finally, our concluding remarks are provided in Section 7.

2. Observations and Data

The observations were acquired using a moored ADCP and two single-point acoustic current meters installed in the bottom layer. These instruments were deployed at Sta. YB in the east of the Yamato Basin during May and October, 2014, and at Sta. TB in the south of the Tsushima Basin during May and October, 2015 (Figure 1 and Table 1).

The upward-looking ADCP (300 kHz, Workhorse, Teledyne RDI) was installed at 2,645 m, and the two single-point current meters (DW-Aquadopp, Nortek AS) were set to 2,560 and 2,475 m at Sta. YB on May

Table 1
Location, Water Depth, Instrument Depth, Instrument Type (AqD: Aquadopp, SG: Seaguard), and Duration of Mooring Observations

Station	Location	Water depth (m)	Instrument depth (m)	Instrument type	Duration
YB	38°17.0′N 135°50.7′E	2,800	2,475	AqD	May 12–June 24, 2014
			2,560	AqD	May 12–July 22, 2014
			2,645	ADCP	May 12–23, 2014
	38°17.0′N 135°51.0′E	2,810	2,656	ADCP	October 16–27, 2014
YB-S	38°15.6′N 135°50.6′E	2,800	950	AqD	October 14, 2013–October 16, 2014
			1,975	AqD	October 14, 2013–October 16, 2014
TB	36°07.0′N 131°14.8′E	1,708	1,417	SG	May 19–June 22, 2015
			1,500	AqD	May 19–July 25, 2015
			1,583	ADCP	May 19–30, 2015
	36°06.8′N 131°14.4′E	1,731	1,414	SG	October 15–November 25, 2015
			1,497	AqD	October 15–November 28, 2015
			1,607	ADCP	October 15–26, 2015

12, 2014 (Figure 2). The ADCP operated for 12 days till May 23 because the batteries ran down, although the measurements of more than 40 days were available from the single-point current meters (Table 1). Therefore, we mainly discuss the flows during the period May 12–23, 2014 as the first set of observations. A similar mooring line was subsequently deployed at Sta. YB for the second set of observations (October 16–27, 2014); however, data from the two single-point current meters could not be obtained owing to instrument failure.

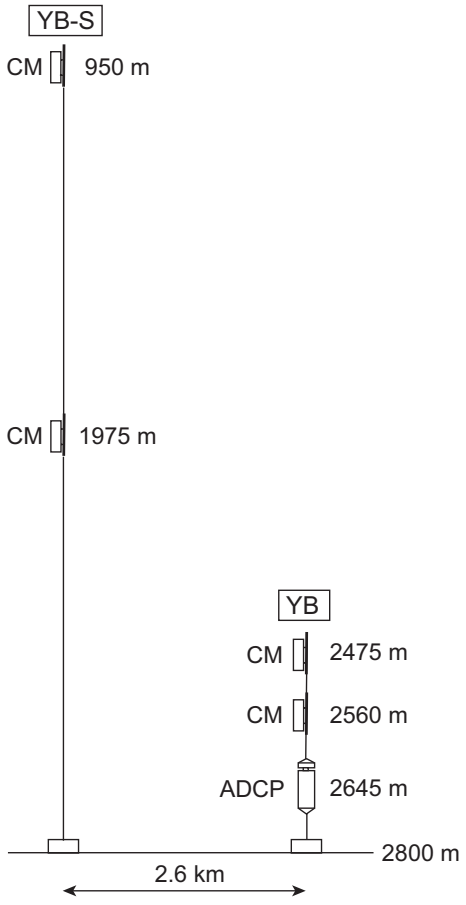

Figure 2. Schematic of the moorings at Stas. YB and YB-S in the Yamato Basin. The instrument labeled "CM" indicates a single-point current meter.

For the first set of observations at Sta. TB in the Tsushima Basin, the ADCP was deployed at 1,583 m, whereas the two single-point current meters (DW-Aquadopp and Seaguard with a ZPulse Doppler current sensor, manufactured by the Aanderaa Data Instruments) were deployed at 1,500 and 1,417 m (Table 1). A similar deployment, but with the ADCP at 1,607 m and two current meters at 1,497 and 1,414 m, was carried out for the second set of observations. All the deployments and recoveries of the instruments were conducted by the T/V Nagasaki Maru of Nagasaki University.

The temporal interval for the measurements at Stas. YB and TB was set to 1 min for all equipment, and the spatial interval for the ADCP was set to 4-m bins. We set the observation range of the ADCP to 100 m; however, no flow data were obtained for layers more than 50 m (60–75 m) apart from the equipment in the Yamato Basin (Tsushima Basin) owing to weak echo intensities. In addition, data from the first bin (6.2 m from the instrument) were noisy.

To reduce short-term fluctuations, a running average of 5 min was applied to the original measurements, following the work of Senjyu (2015). After this operation, the nominal standard deviation of the ADCP measurement was 0.32 cm s^{-1}; however, noisy fluctuations tended to increase with increasing distance from the equipment. The nominal accuracies of the current speed for the Aquadopp and Seaguard instruments were 1% of the measured values ±0.5 and ±0.15 cm s^{-1}, respectively.

In addition to the above observations, two current meters (DW-Aquadopp) were deployed at 950 and 1,975 m of Sta. YB-S (south of Sta. YB), which were 2.6 km apart, during the period from October 14, 2013 to

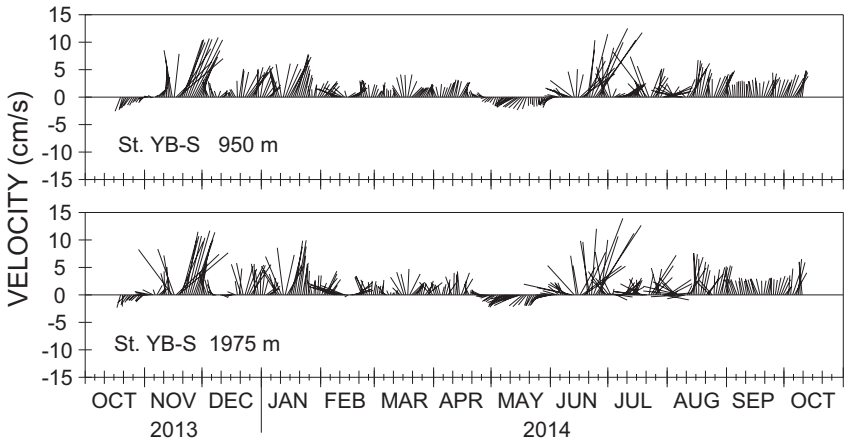

Figure 3. Stick diagrams of the flows at 950 and 1,975 m of Sta. YB-S during the period from October 19, 2013 to October 11, 2014. Daily flow data after 48-h low-pass filtering are plotted.

October 16, 2014 (Figure 2 and Table 1). The bottom topography around the mooring sites is relatively flat (Figure 1c). The year-round measurements from the current meters demonstrated that Sta. YB-S and possibly Sta. YB are located in an area of dominant northward flows, although southwestward flows prevailed during the first set of observations in May 2014 (Figure 3). The northward flows at Sta. YB-S are part of the cyclonic circulation in the Yamato Basin (Senjyu, Shin, et al., 2005). We analyzed the data from Sta. YB-S together with the measurements obtained from Sta. YB, although the measurement interval for the current meters at Sta. YB-S was set to 30 min.

A hydrographic observation with a conductivity-temperature-depth profiler (CTD) (SBE 911+, Sea-Bird Scientific) was conducted at Sta. TB on May 19, 2015 to investigate stratification conditions at the mooring site. However, as we have no hydrographic data at Sta. YB during the mooring observations, the stratification near Stas. YB and YB-S was determined from the mean density profiles at Stas. KS4044 and KS4315, which were observed on November 9, 2013 and September 26, 2014, respectively, by the Japan Meteorological Agency (JMA) (Figure 1c) (Japan Meteorological Agency, 2013, 2014). In addition, the wind data from the Grid Point Value/Meso Spectral Model (GPV/MSM) by the JMA are analyzed. The GPV/MSM provides hourly operational weather forecasting data with latitudinal and longitudinal spatial resolutions of 0.05° and 0.0625°, respectively.

3. Results

3.1. Yamato Basin

Clear sinusoidal variations of periods ~20 h were observed in the flows at each layer in the sets of observations from May and October, 2014, although their amplitudes varied temporally (Figure 4). A clockwise change in the flow direction can be inferred from the phase lag of approximately 90° in the east–west component of the flow (u) compared with the north–south component (v). In fact, the rotary spectra of the flows in both sets of observations exhibited a significant energy peak near the local inertial frequency f at Sta. YB ($f_{YB} = 0.903 \times 10^{-4}$ rad s^{-1}) in the clockwise component only (Figure 5). For the calculation of spectra, the technique of fast Fourier transform with a triangular filter of degrees of freedom 9 for the averaging in frequency domain was used. Similar spectra were observed in other layers (not shown). Therefore, the flows in the abyssal Yamato Basin were dominated by NIWs, as highlighted in previous studies (Mori et al., 2005; Senjyu, 2015; Senjyu, Shin, et al., 2005).

Of particular interest is the amplitude variation of the inertial flows. During the first observational period in May, an inertial variation with an amplitude of approximately 5 cm s^{-1} was clearly observed from May 12 to 16 throughout the observed layers (Figure 4a). However, after this period, the inertial variation weakened abruptly and remained insignificant until May 18. The inertial variation recovered after May 19; however, its amplitude remained at approximately one-third of that during May 12–16. The significant amplitude

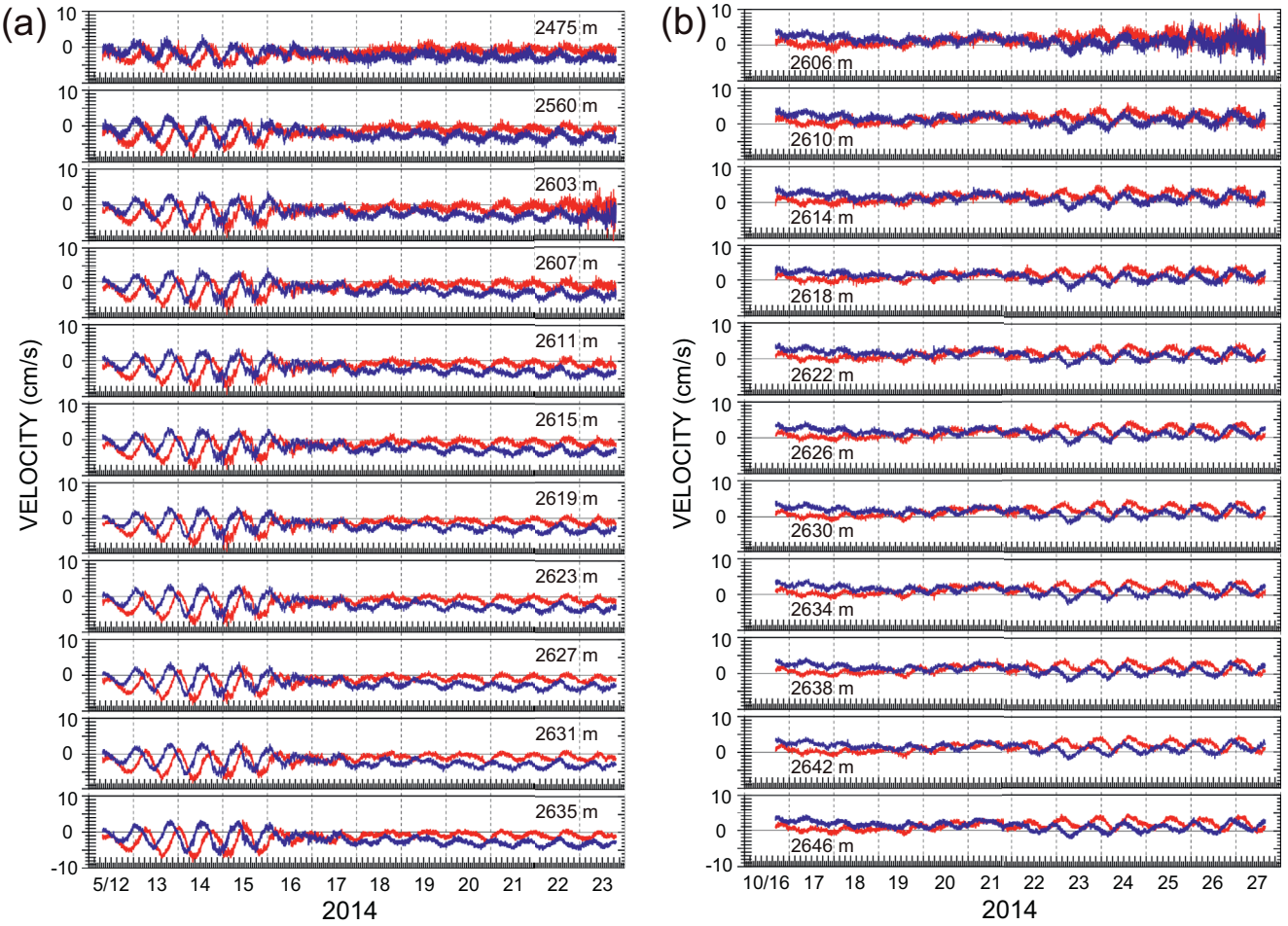

Figure 4. Time series of the zonal (u, red) and meridional (v, blue) components of the flows during (a) May 12–23 and (b) October 16–27, 2014 at Sta. YB.

observed during May 12–16 suggests that a wave packet of NIWs arrived at Sta. YB in this period. We will discuss this distinctive period in the next section. A similar amplitude modulation was found in the second set of observations; the inertial variation had an amplitude of approximately 3 cm s^{-1} during the period October 23–27, following the inactive period of October 16–21 (Figure 4b).

3.2. Tsushima Basin

In contrast to the Yamato Basin, the flows in the abyssal Tsushima Basin exhibited more complex changes than a simple sinusoidal variation (Figure 6). During both May and October, 2015, the time series of u and v exhibited one or two peaks (troughs) per day throughout the layers, suggesting a linear combination of multiple sinusoidal variations. The rotary spectra based on the measurements of the single-point current meters that operated longer than the ADCP showed three frequencies of significant energy: near the local inertial frequency f at Sta. TB ($f_{TB} = 0.859 \times 10^{-4}$ rad s^{-1}) in the clockwise component, the diurnal frequency in the anticlockwise component, and the semidiurnal frequency in both clockwise and anticlockwise components (Figure 7).

The energy peak at the near-inertial frequency in the clockwise component can be associated with NIWs, whereas the peaks at the diurnal (K_1) and semidiurnal (M_2) frequencies are due to the tidal waves from the East China Sea, where the tidal amplitude is significant. Senjyu, Shin, et al. (2005) also reported spectral peaks at O_1, K_1, M_2, and S_2 frequencies from an abyssal flow data set in the southern Tsushima Basin obtained over a one-year period. As the diurnal frequency is lower than the local inertial frequency at Sta. TB, the diurnal tidal waves behave as boundary-trapped waves. In contrast, the semidiurnal tidal waves can

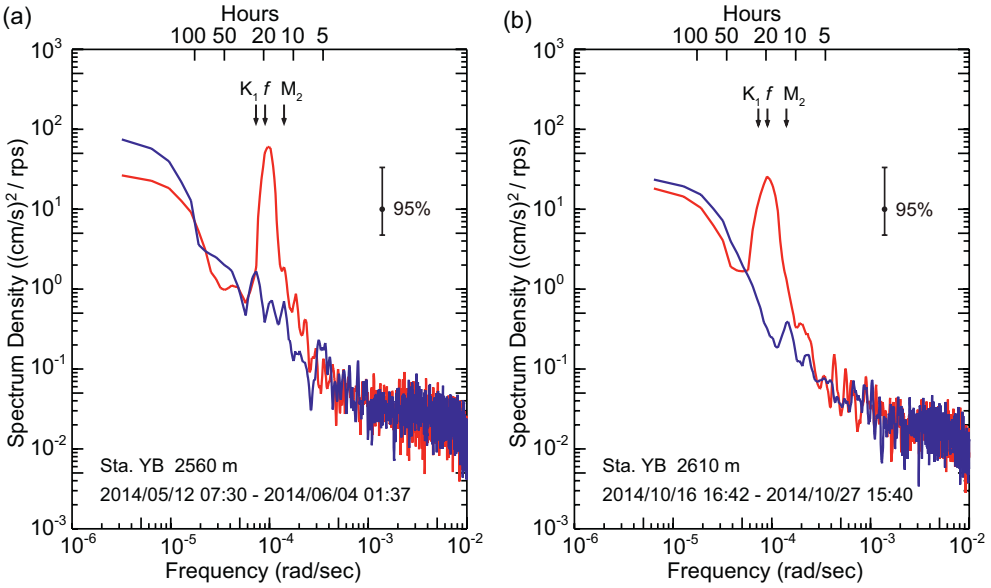

Figure 5. Rotary spectra of the flows for Sta. YB, (a) at 2,560 m in May and (b) at 2,610 m in October 2014. The red and blue lines indicate the clockwise and anticlockwise components, respectively. The arrows f, K_1, and M_2 indicate the frequencies of local inertial, K_1, and M_2 tidal constituents, respectively. Note that the spectra in (a) were calculated from a data set from May12 to June 4 to increase frequency resolution.

propagate freely everywhere. The reason for the difference between the energy peak at K_1 frequency in the anticlockwise component only and that at M_2 frequency in both clockwise and anticlockwise components is due to the difference in the wave characteristics of diurnal and semidiurnal waves (Park & Watts, 2006).

4. Significant Events of NIWs in the Yamato Basin

First, we focus on the significant NIW event during the period May 12–16, 2014 at Sta. YB. To extract the inertial components of u and v (hereafter, u_i and v_i, respectively), we applied a fourth-order Butterworth band-pass filter with the bandwidth of $0.90–1.20f_{YB}$ to the data set (Figure 8a). The filter was applied twice to the data set, once forward and then backward, to minimize distortion and phase shift using the filtering operation, after the appendance of the dummy data (filled by zero) of 50 h period-long to the end of the data sets (Ito & Minobe, 2010). The time series of u_i and v_i at representative depths are shown in Figure 9a.

The time-depth diagrams of u_i and v_i during the NIW event show the near-inertial flows with a vertically coherent phase throughout the depths (Figures 10b and 10c). We defined the core period of the NIW event from 00:00 on May 13 to 05:00 on May 16, 2014 (77 h, approximately 4 times the local inertial period), and then estimated the dominant frequency (ω_i) in u_i and v_i during the event by autocorrelation method (Table 2). The estimated frequency 0.966×10^{-4} rad s^{-1} showed a slight blue-shift ($1.07f_{YB}$), similar to other oceans (Alford, MacKinnon, Simmons, & Nash, 2016). Another noticeable feature during the event is flow intensification with depth (Figure 10a). In fact, the mean velocity during the core period of the event showed a significant increase with depth by a factor of 1.5, from 1.94 cm s^{-1} at 2,475 m to 2.98 cm s^{-1} at 2,635 m (Table 3 and Figure 11a).

Similar events to that at Sta. YB with remarkable NIWs occurred at 1,975 and 950 m of Sta. YB-S during the periods May 13–16 and May 14–17, 2014 respectively, suggesting an upward propagation of a wave packet (Figure 12). Furthermore, if we regarded Stas. YB and YB-S as a single station, the wave packet of NIWs during May 12–16 at 2,475 m appears to propagate upward to 1,975 m. The speeds of the upward propagation of the wave packet were roughly estimated using cross-correlations between current speeds $\left(u_i^2 + v_i^2\right)^{1/2}$ at 2,475 and 1,975 m (1,975 and 950 m) for the period from 07:30 on May 12 to 23:00 on May 17 (from 00:00 on May 13 to 23:30 on May 17). The speed calculated from the distance between 2,475–1,975 m

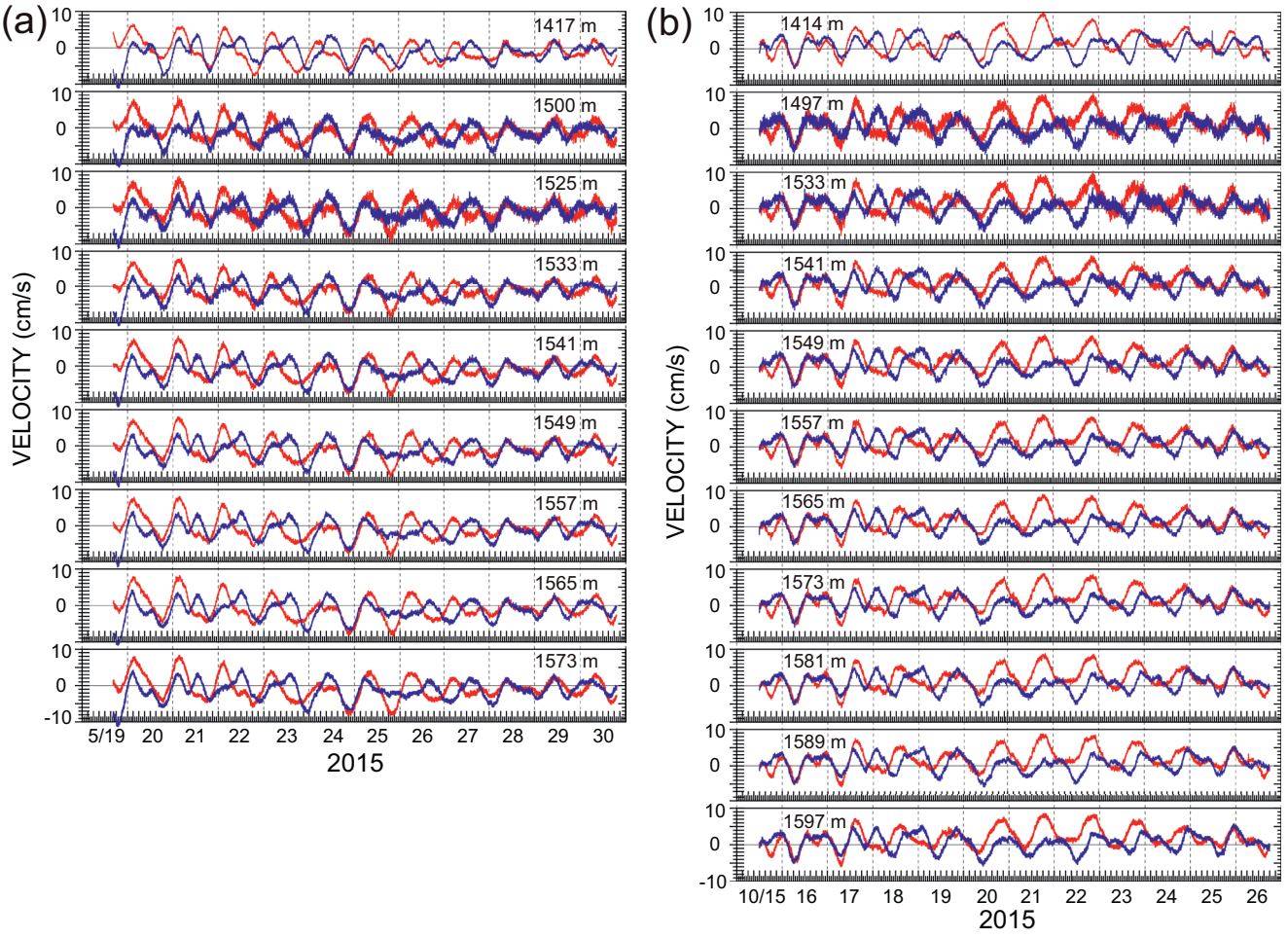

Figure 6. Time series of the zonal (u, red) and meridional (v, blue) components of the flows during (a) May 19–30 and (b) October 15–26, 2015 at Sta. TB. For the ADCP measurements, flows at 8-m intervals are shown.

(1,975–950 m) divided by the time lag at a maximum correlation is 0.75 (1.39) cm s^{-1}. These values are 10–1,000 times larger than the values of vertical component of the group velocity (Cg_z) reported in the upper layers (~800 m) of the North Pacific (Alford, Cronin, & Klymak, 2012). However, considering the very weak stratification in the abyssal Japan Sea and uncertainty in the detection of cross-correlations peak, the estimated wave packet speeds are not so extraordinary (see Appendix A).

The upward energy propagation suggests that the observed NIWs were generated at the seabed or were bottom-reflected waves. Nikurashin and Ferrari (2010a, 2010b) showed that NIWs can be excited by the geostrophic flows impinging on the bottom topography. The southwestward flows that prevailed in May 2014 at Sta. YB-S (Figure 3) and small sea mountains to the north of the mooring sites (Figure 1c) imply the influence of the lee waves generated by the interaction of the deep flow with the bottom topography. However, the NIW events occurred intermittently at Sta. YB during the observation period (Figure 12), although the southwestward flows occurred throughout May 2014. The main energy source of NIWs in the Japan Sea is wind over the sea (Mori et al., 2005). Although most of the wind energy input into the ocean is confined and dissipates within the surface mixed layer (Alford, Cronin, & Klymak, 2012; Furuichi et al., 2008), part of the energy can propagate to the depths as NIWs that could be reflected upward from the seabed (Garrett, 2001). The wind conditions during the period from two weeks before to the end of the observations were analyzed on the basis of the GPV/MSM data set (Figure 13). Considering the observed NIW frequency ($1.07f_{YB}$), the area-mean wind to the north of the stations (40.5°N-42.5°N, 135°E-137°E) were examined. The critical latitude where the inertial frequency matches $1.07f_{YB}$ is 41.5°N. In addition, the wind energy

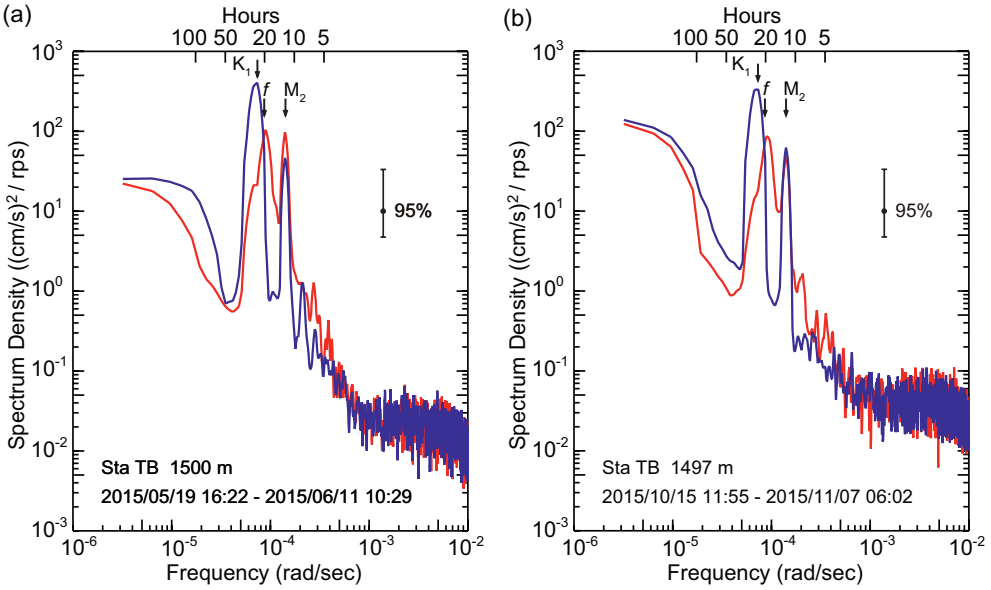

Figure 7. Same plots as Figure 5 for Sta. TB, (a) at 1,500 m in May and (b) at 1,497 m in October 2015. The spectra in (a) and (b) were calculated from the data sets during the periods May 16–June 11 and October 15–November 7, respectively, to increase frequency resolution.

flux into inertial motions in the surface mixed layer was estimated by the slab model (D'Asaro, 1985; Pollard & Millard, 1970), using the wind stress based on Large and Pond (1981). The wind events on May 3 and 5 appears to correspond to the NIW event occurred at 950 m of Sta. YB-S for the period May 10–12, although a corresponding NIW event was not observed at 1,975 m (Figure 12). A closer examination reveals, however, that there were slight phase lags by 210 and 300 min in u_i and v_i at 950 m, respectively, compared with those at 1,975 m (i.e., upward phase propagation) during the period May 10–12. This may indicate a downward energy propagation of NIWs prior to the NIW event at Sta. YB during May 12–16.

5. Spatiotemporal Variations of NIW Amplitude

The time series of u_i and v_i at representative layers in all the observations are shown in Figure 9. The same filtering procedure explained in the previous section was applied to the second set of observations at Sta. YB in October 2014. However, a sixth-order band-pass filter with the bandwidth of $0.95–1.20f_{TB}$ was applied to the data sets from Sta. TB (Figure 8b), after the appendance of dummy data of 100 h period-long, to isolate the near-inertial component from the tidal motions. The filter response function of the applied band-pass filter anticipated an effective separation of the inertial motion from the K_1 and M_2 tidal constituents. In fact, the near-inertial motions with a clockwise change in the flow direction due to NIWs are clearly exhibited in the time series of u_i and v_i (Figures 9c and 9d).

The amplitude variations of u_i and v_i in time and space are of particular interest. Remarkable near-inertial flows occurred at Sta. TB during the periods May 24–28 and October 15–19, 2015, as well as a weaker event during October 22–27, 2014 at Sta. YB (Figure 9). We defined the core periods of each NIW event as the first set of observations at Sta. YB, and then estimated the dominant frequencies ω_i during the events (Table 2). The estimated frequencies showed slight blue shift in all the cases: $1.01f_{YB}$ for Sta. YB in October 2014 and $1.05f_{TB}$ for both May and October 2015 at Sta. TB.

The wind conditions before and during the observations are shown in Figure 13. As the critical latitudes for the dominant frequencies ω_i at Sta. YB in October 2014 and Sta. TB in 2015 are 38.9°N and 38.3°N, respectively, corresponding area-mean winds (38°N-40°N, 135°E-137°E and 37.5°N-39.5°N, 130°E-132°E) were examined (Table 2). Although the one-to-one correspondence between wind and NIW events are unclear, relatively strong wind prior to NIW events were confirmed (e.g., May 20–23 and October 10 and 12 in 2015 for Sta. TB, along with May 3–5 in 2014 for Sta. YB-S discussed in the previous section).

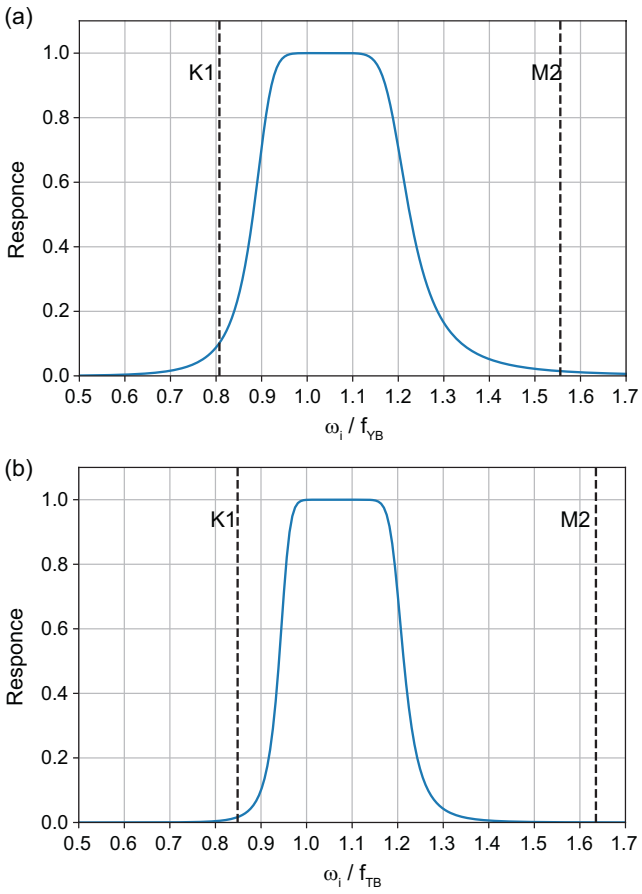

Figure 8. Filter response functions of the Butterworth band-pass filter applied to the data from (a) Sta. YB and (b) Sta. TB. Frequencies in the horizontal axis are normalized by the local inertial frequency at each station. The K_1 and M_2 tidal frequencies are indicated by dashed lines.

The time-depth diagrams of flow for the NIW events observed at Sta. TB in May and October 2015 are shown in Figures 14 and 15, respectively. The near-inertial flows with almost constant phase throughout the depths occurred during both events, although slight upward phase propagations in u_i and v_i appeared in the initial stage of the event in May 2015 (Figures 14b and 14c). The flow was intensified with depth in the event of May 2015 (Figure 14a), as the case in May 2014 at Sta. YB (Figure 10a). However, the flow in October 2015 showed a maximum in the intermediate layer ranging 1,497–1,561 m (Figure 15a). To see the varying flow amplitude with depth, the profiles of mean velocities for the core period of each event are plotted (Figure 11). At Sta. YB, a remarkable flow intensification with depth was observed in May 2014 as described in the previous section, whereas weaker flows of 1.2–1.3 cm s^{-1} were observed in October 2014 (Figure 11a). In contrast, in the event of October 2015 at Sta. TB, the velocity amplitude decreased with depth from 1.73 cm s^{-1} at 1,561 m to 1.44 cm s^{-1} at 1,597 m (Figure 11b). The maximum amplitude was 1.76 cm s^{-1} at 1,497 m, above the layer of almost constant amplitude (1.71–1.76 cm s^{-1}) ranging 1,497–1,561 m. A similar layer of constant flow amplitude (2.04–2.08 cm s^{-1}) occurred in the range 1,549–1,573 m in May 2015 at Sta. TB.

It is noteworthy that in the observations of May 2015 at Sta. TB (Figure 9c), the NIW event at 1,417 m appeared to begin from May 22, about 0.5 days earlier than the deeper layers where the near-inertial flows intensified from May 23. This suggests a downward energy propagation of NIWs prior to the main NIW event in the deeper layers, together with the upward phase propagation in the initial stage of the event (Figures 14b and 14c).

6. Discussion

The analysis based on vertical normal mode expansion has revealed that NIWs in the interior ocean propagate horizontally as a low mode internal waves (Alford, 2003a; Furuichi et al., 2008). Indeed, Watanabe and Hibiya (2018) showed that the deep flow field in the northern Japan Sea in response to surface wind events can be reproduced by a two-layer model that allows first-mode internal wave only. Under the hydrostatic approximation, we determined the vertical structure of horizontal flow accompanied by normal mode internal waves based on the observed density stratifications (Cushman-Roisin & Beckers, 2011). Reflecting the weak stratification in the abyssal Japan Sea (Figures 16a and 16c), the profiles of horizontal flow of first-mode internal wave show almost constant amplitude below 1,000 m in both the Yamato and Tsushima Basins (Figures 16b and 16d). Although higher-mode profiles of horizontal flow exhibit a slight increase of amplitude with depth below 1,000 m, they cannot explain the observed flow profiles, in particular a maximum and decrease of flow amplitude with depth at Sta. TB in October 2015 (Figure 11).

A plausible explanation for the observed flow characteristics is superposition of upward- and downward-propagating NIWs. The schematics of flow fields in upward- and downward-propagating NIWs is shown in Figure 17 on the basis of the polarization relations of internal gravity waves in a rotating frame (Gill, 1982). Horizontal flow accompanied by a downward-propagating NIW shows a clockwise rotation of flow direction with increasing depth (Figure 17b). On the other hand, the flow accompanied by the upward-propagating NIW, which was the downward-propagating NIW bounced off the seabed, rotates anti-clockwise with increasing depth (Figure 17a). Near the seabed, both NIWs could interfere each other to set up a standing wave (Figure 17c). To satisfy the bottom boundary condition that the normal component of the flow is zero at the boundary, the amplitude of the horizontal flow is set to a maximum at the seabed (loop) (Figure 18). The horizontal flow accompanied by the superposed NIWs decreases with height from

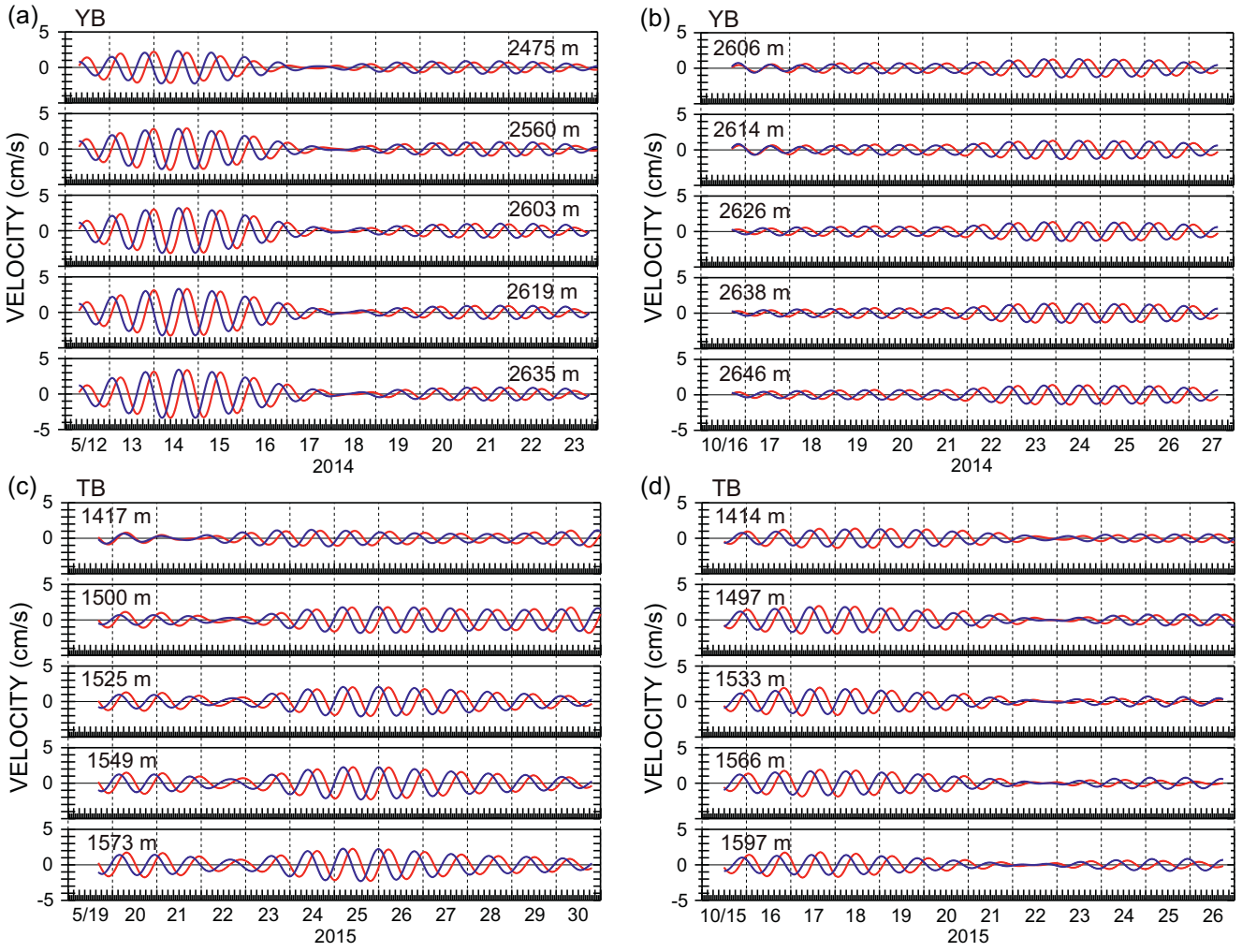

Figure 9. Time series of the band-pass filtered flows at the representative depths (a) in May 2014 at Sta. YB, (b) in October 2014 at Sta. YB, (c) in May 2015 at Sta. TB, and (d) in October 2015 at Sta. TB. The red and blue lines in each panel indicate the zonal (u_i) and meridional (v_i) components, respectively.

the bottom, and then the flow of opposite direction occurs above the level of no horizontal flow (node) at a quarter of the vertical wavelength ($\lambda_z/4$) from the bottom. Above that, loop and node occur alternately. The flow at a fixed depth rotates clockwise with time following the upward and downward phase propagations of the incident and reflected waves, respectively, preserving its amplitude; however, phase of the flow between nodes is vertically coherent.

To demonstrate this situation, we formally decomposed u_i and v_i during each NIW event into the upward- and downward-phase-propagating components (i.e., downward- and upward-propagating NIWs, respectively) using 2D-Fourier transform method (Lien et al., 2013). The amplitude of decomposed velocities in both u_i and v_i during the event at Sta. YB in May 2014 are almost identical and the flow intensification with depth was caused by the superposition of upward- and downward-phase-propagating NIWs (Figure 10). In addition, the mean amplitude of decomposed velocities for the NIW event (1.43–1.55 cm s^{-1}) were comparable to those at 950 and 1,975 m of Sta. YB-S (1.44–1.76 cm s^{-1}) before and after the NIW event in the deeper layers (Table 3). This supports the idea that the significant NIWs observed at Sta. YB in May 2014 were the result of the superposition of the downward wind-generated NIW and upward reflected NIW. By contrast, for the event at Sta. TB in May 2015, the flow intensification near the bottom appears to be composed by the bottom-intensified upward- and downward-propagating waves (Figure 14). The middepth maximum of flow amplitude during the event at Sta. TB in October 2015 was formed by the superposition of downward-phase-propagating wave accompanying strong flow layer around 1,550 m and weaker

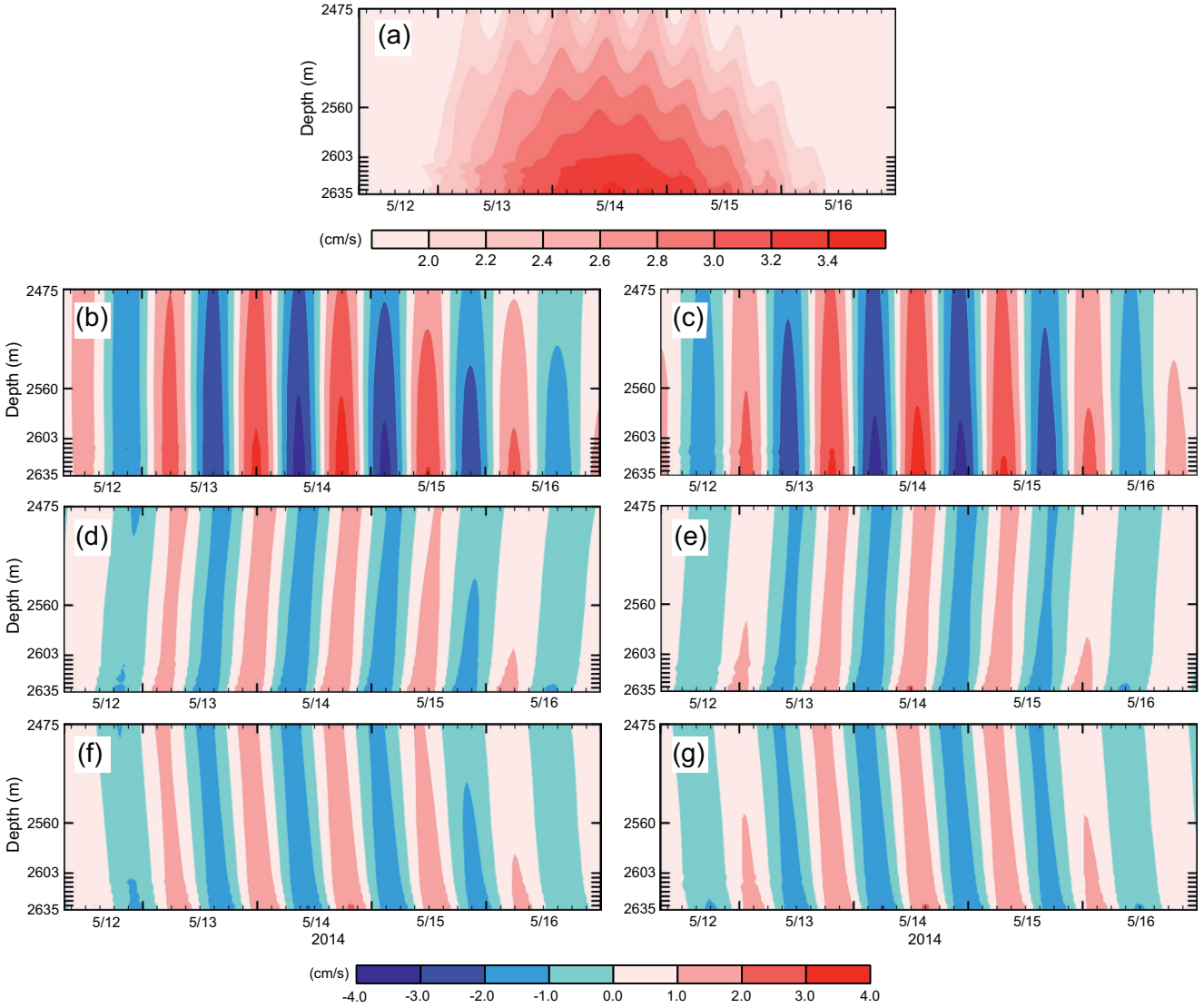

Figure 10. Time-depth diagrams of the band-pass filtered flow at Sta. YB during the period 08:00 on May 12 to 00:00 on May 17, 2014: (a) flow speed $\left(u_i^2 + v_i^2\right)^{1/2}$, (b) zonal flow ($u_i$), (c) meridional flow ($v_i$), (d) upward-phase-propagating component of u_i, (e) upward-phase-propagating component of v_i, (f) downward-phase-propagating component of u_i, and (g) downward-phase-propagating component of v_i.

upward-phase-propagating waves (Figure 15). The complicated flow structure at Sta. TB may associate with the steep bottom topography south of the mooring site (Figure 1b), such as the wave reflection at the southern rim of the basin.

Table 2
Core Period and ω_i (Mean ± Standard Deviation) for the NIW Events

Station	Depth (m)	Core period of NIW event	ω_i (10^{-4} rad s^{-1})
YB	2,475–2,635	00:00 May 13–05:00 May 16, 2014	0.966 ± 0.002
	2,606–2,646	09:00 October 23–14:00 October 26, 2014	0.916 ± 0.003
TB	1,417–1,573	06:00 May 24–15:00 May 27, 2015	0.901 ± 0.007
	1,414–1,597	06:00 October 16–15:00 October 19, 2015	0.906 ± 0.009

Note. The core periods were taken for 77 and 81 h for Stas. YB and TB, respectively, which is approximately four times the local inertial period.

Table 3

Mean ± Standard Deviations of Velocity Amplitudes $\left(u_i^2 + v_i^2\right)^{1/2}$ *During the Core Period of NIW Event in May 2014 at Stas. YB and YB-S*

Station	Depth (m)	Core period of NIW event	Amplitude (mean ± sd) (cm s^{-1})
YB-S	950	12:00 May 10–00:00 May 13	1.44 ± 0.09
		12:00 May 14–17:00 May 17	1.76 ± 0.10
	1,975	19:00 May 13–00:00 May 17	1.61 ± 0.06
YB	2,475	00:00 May 13–05:00 May16	1.94 ± 0.34
	2,560	00:00 May 13–05:00 May16	2.56 ± 0.34
	2,603	00:00 May 13–05:00 May16	2.80 ± 0.36
	2,607	00:00 May 13–05:00 May16	2.83 ± 0.36
	2,611	00:00 May 13–05:00 May16	2.87 ± 0.37
	2,615	00:00 May 13–05:00 May16	2.89 ± 0.37
	2,619	00:00 May 13–05:00 May16	2.90 ± 0.37
	2,623	00:00 May 13–05:00 May16	2.93 ± 0.38
	2,627	00:00 May 13–05:00 May16	2.94 ± 0.38
	2,631	00:00 May 13–05:00 May16	2.98 ± 0.38
	2,635	00:00 May 13–05:00 May16	2.98 ± 0.39

It is important to note that, for our data sets, the vertical wavelength of upward- and downward-phase-propagating waves cannot be determined correctly from the decomposed flow fields. Since the 2D-Fourier transform method formally separates upward- and downward-phase-propagating components on the basis of temporal and spatial variabilities in the observed flow field, the spatial information obtained from vertically coherent flow throughout the observational depth range such as our data sets is unreliable. Indeed, the vertical wavelengths estimated from the decomposed flows using the method of Senjyu (2015) based on the wave polarization were in a range of 640–870 m, about four times the observation range, regardless of the observation time and area. Therefore, we try to evaluate the vertical wavelength of NIW during the events by a comparison between the observed and conjectural flow amplitudes. The positions of flow measurement in each observation are plotted along with the profile of horizontal flow amplitude that occurs when a downward- and upward-propagating NIWs were superimposed (Figure 18). These positions of flow measurement were scaled by an arbitrarily selected vertical wavelength (λ_z) accounting for the observed flow amplitudes (Figure 11). The maximum at 1,497 m and decreasing amplitude below 1,561 m at Sta. TB in October 2015 are ascribed to the loop and node at $\lambda_z/2$ and $\lambda_z/4$ from the bottom, respectively, when the vertical wavelength λ_z is 450 m (Figure 11b). Similarly, the maximum amplitude at 1,549 m in May 2015 at Sta. TB is attributable to the loop at $\lambda_z/2$ when $\lambda_z = 320$ m, although there is a discrepancy that the flow at 1,417 m above the second node at $3\lambda_z/4$ did not show opposite direction to that in lower layers (Figure 9c). On the other hand, the flow amplitude at Sta. YB monotonically increased with depth (Figure 11a). Since the phase of the observed flow was vertically coherent throughout the depths (Figures 9a and 10), it is suggested that all the current meters were within the range between the bottom and first node at $\lambda_z/4$. This indicates that the NIWs observed at Sta. YB during the event of May 2014 had a vertical wavelength of more than 1,400 m.

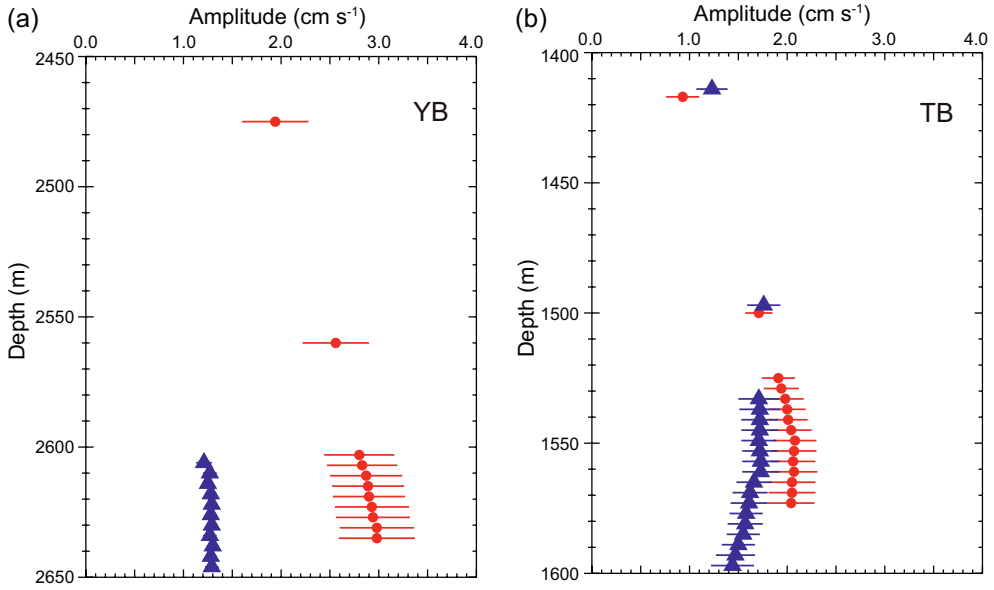

Figure 11. Vertical distributions of the velocity amplitude for the core periods of each NIW event at (a) Sta. YB and (b) Sta. TB. The red circles and blue triangles in each panel are for the observations in May and October, respectively. Horizontal bars at each symbol denote standard deviations.

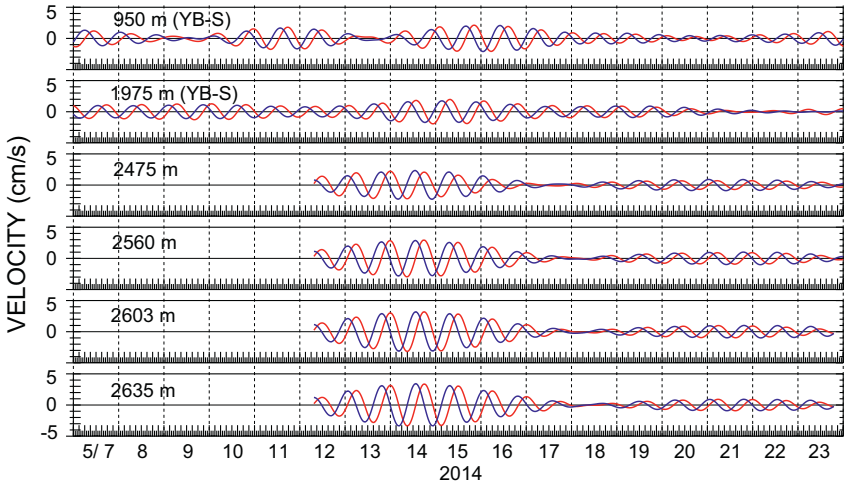

Figure 12. Time series of the band-pass filtered flows at the representative depths during the period May 7–23, 2014: from the top panel, 950 and 1,975 m at Sta. YB-S and 2,475, 2,560, 2,603, and 2,635 m at Sta. YB. The red and blue lines indicate the zonal (u_i) and meridional (v_i) components, respectively.

As the stratification in the abyssal Japan Sea, particularly below 2,000 m, is very weak (Fig. 16a), a slight vertical shear due to NIWs superposition can induce an unstable condition that promotes vertical mixing. The time-depth diagram of the Richardson number ($\mathrm{Ri} = N^2/S^2$) at Sta. YB in May 2014 based on the vertical shear $S^2 = (\partial u_i/\partial z)^2 + (\partial v_i/\partial z)^2$ and the constant profile of N (Figure 16a) is shown in Figure 19. Unstable conditions ($\mathrm{Ri} < 0.25$) lasting a few hours occurred sporadically during the initial stage of the NIW event (May 12–13) below 2,607 m. In addition, relatively small values ($0.25 < \mathrm{Ri} < 10$) occurred during the periods May 13–16 and 21–23 for the layers 2,475–2,635 m and 2,560–2,635 m, respectively. These periods coincide with the periods of active NIWs (Figure 9a). This suggests the activation of vertical mixing in the deep sea during significant NIW events, although the modulation of Ri is sensitive to temporal variations in N (Alford & Gregg, 2001).

7. Concluding Remarks

NIWs in the abyssal Yamato and Tsushima Basins in the Japan Sea were investigated using the mooring observations. The significant NIW events of 3–5 days occurred intermittently in both basins. The near-inertial flows with the characteristics of a vertically coherent phase and varying amplitude with depth were observed in all the NIW events. These flow characteristics can be explained by the superposition of upward- and downward-propagating NIWs. This idea is consistent with the report of the lowered ADCP observations in the Japan Sea by Shcherbina et al. (2003). They showed that the upward- and downward-propagating internal waves equivalently contribute to the rise of the total kinetic energy below 2,000 m. A cause of the unrealistic vertical wavelength of NIW estimated by Senjyu (2015) which is larger than the water depth is without consideration of the NIWs superposition. Although we have estimated the vertical wavelengths assuming the superposition of NIWs in this study, long-range observations over several hundred meters from the seabed with sufficient spatial resolution are desired for the exact estimation of vertical wavelength of NIWs in the deep ocean.

In addition, the promotion of vertical mixing in the deep sea during significant NIW events was suggested. Vertical mixing caused by the superposition of NIWs may partly contribute to the formation and/or maintenance of the Japan Sea Bottom Water which is characterized by an extreme vertical homogeneity of water characteristics (Gamo & Horibe, 1983; Gamo et al., 1986; Senjyu, Isoda, et al., 2005). The intermittent nature of NIW events explains the low turbulent dissipation rate in the Bottom Water obtained from the direct turbulent observations (Matsuno et al., 2015).

The proposed mechanism of the deep flow intensification due to the superposition of NIWs is likely to be a general oceanic phenomenon. Strictly speaking, as the group velocity of NIW has a horizontal component,

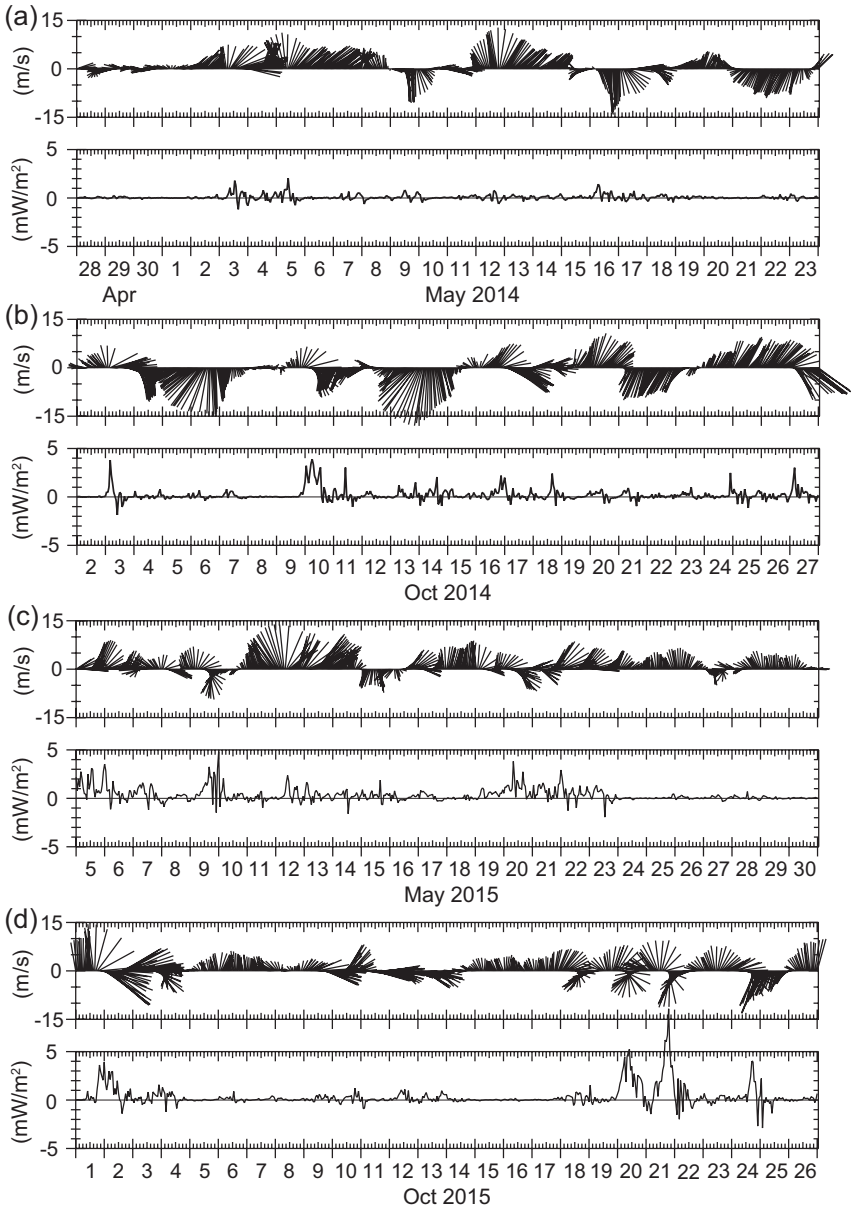

Figure 13. Stick plots of the wind (upper) and wind energy flux (lower) before and during the observations: (a) at Sta. YB in April–May 2014, (b) Sta. YB in October 2014, (c) Sta. TB in May 2015, and (d) Sta. TB in October 2015. The area-mean winds over the regions corresponding to ω_i are plotted. The wind energy flux was estimated by the slab model (D'Asaro, 1985) assuming the mixed layer depth of 50 m and damping constant of $f/2\pi$.

the raypath of the reflected waves does not coincide with that of the incident waves (Figure 20). However, NIWs are probably excited in a wide area of the upper ocean due to a strong wind event, considering the horizontal scale (several hundred kilometers) and migration speed (few tens kilometers per hour) of atmospheric disturbances. The energy of NIWs propagate downward and equatorward along rays, and then bounce off the seabed (Garrett, 2001). In the situation that multiple rays concurrently exist in a local area, the superposition between rays of reflected and adjacent incident waves is expected. The NIW rays could be influenced significantly by the vorticity distribution in the course of the propagation (e.g., Kawaguchi et al., 2020; Kunze, 1985; Oey et al., 2008). The vague correlation between the wind and NIW events may be attributable to mesoscale eddies in the upper ocean which was not discussed in this study. Our discussion was based on the single mooring observations with relatively short durations. To clarify the horizontal scale,

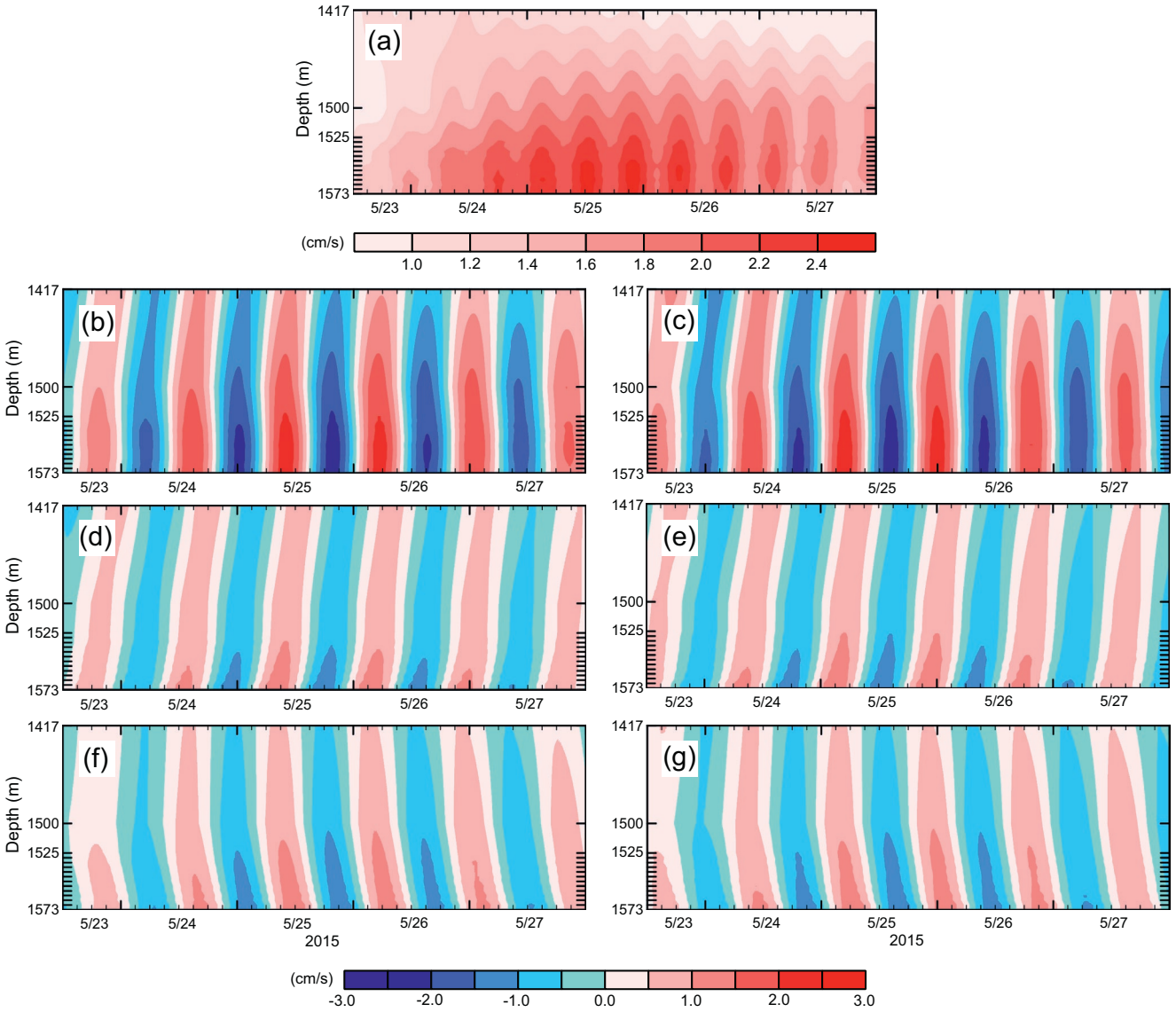

Figure 14. Same plots as Figure 10 for Sta. TB during the period 12:00 on May 23 to 00:00 on May 28: (a) flow speed, (b and c) u_i and v_i, (d and e) upward-phase-propagating components of u_i and v_i, and (f and g) downward-phase-propagating component of u_i and v_i, respectively.

duration, and frequency of occurrence of the strong flows in the deep sea, further analyses of long-term data from multiple locations are required.

Appendix A: Change of the NIW Wavenumbers During the Propagation

The aspect ratio of internal waves (a) with a fixed frequency ω is given by

$$a^2 = \frac{m^2}{k^2 + l^2} = \frac{N^2 - \omega^2}{\omega^2 - f^2}, \tag{1}$$

where k, l, and m denote the zonal, meridional, and vertical wavenumbers, respectively (Gill, 1982). The profile of the aspect ratio at Sta. YB (TB) assuming $f = f_{YB}$ (f_{TB}) and observed frequency $\omega = \omega_i$ shows that a varies from 2–4 below 2,300 m to approximately 400 at 50 m via 100 around 250 m (Figure A1). The small values of a in the deep layer are owing to the extremely narrow temperature and salinity ranges of the Japan Sea Proper Water (Worthington, 1980; Yasui et al., 1967). While, the value $a = 100$ at 250 m means that a

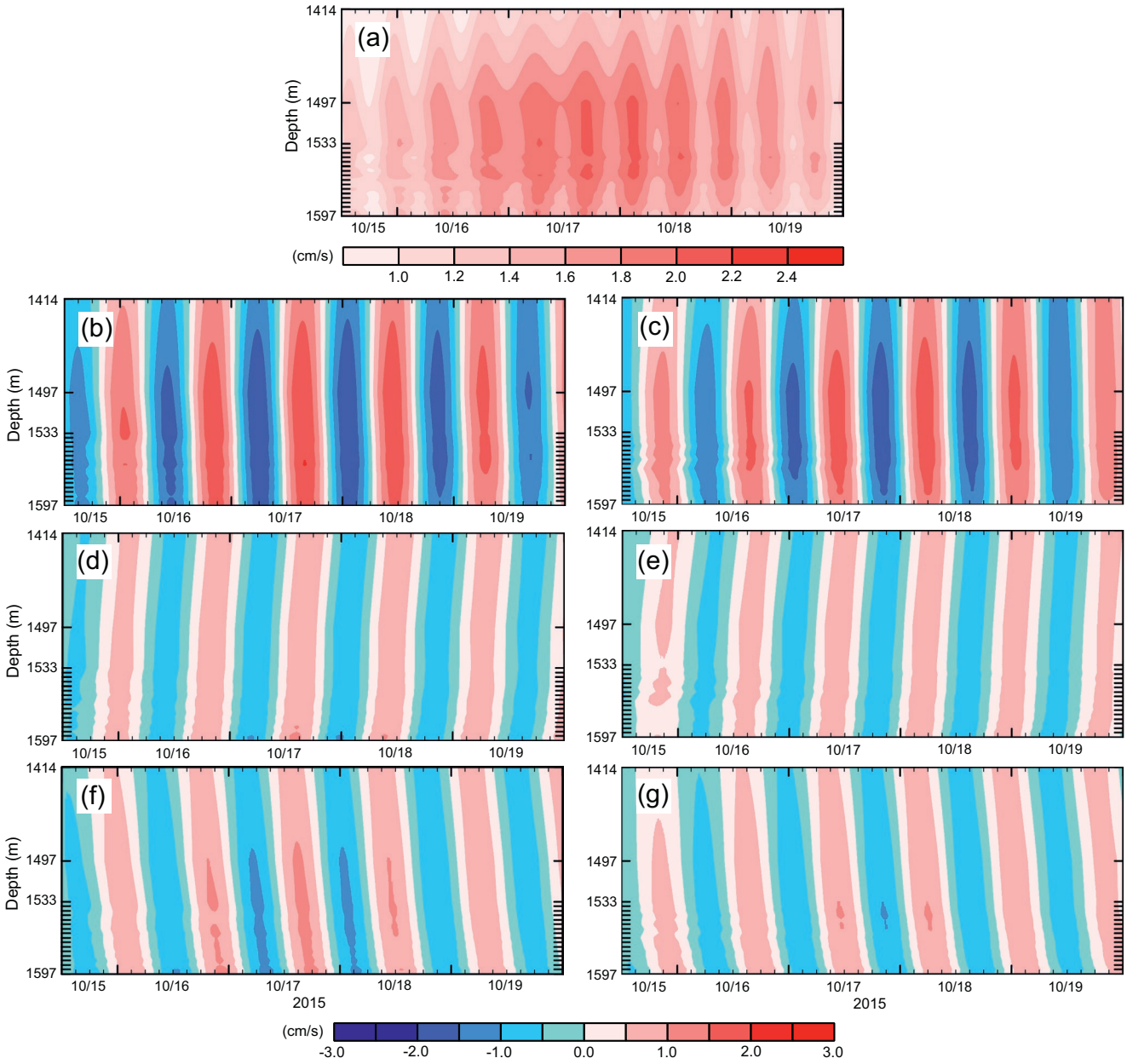

Figure 15. Same plots as Figure 10 for Sta. TB during the period 12:00 on October 15 to 00:00 on October 20: (a) flow speed, (b and c) u_i and v_i, (d and e) upward-phase-propagating components of u_i and v_i, and (f and g) downward-phase-propagating component of u_i and v_i, respectively.

NIW with a horizontal wavelength of 30 km just under the main thermocline have a vertical wavelength of 300 m. When the NIW propagates to 2,500 m along a raypath preserving its frequency, the horizontal and vertical wavelengths continuously change following the profile of a.

To examine the origin of the NIWs observed at Sta. YB in May 2014 and changes in wavenumber (wavelength) during the propagation, we performed several ray-tracing experiments of NIW on the β-plane ($f = f_0 + \beta y$) based on the ray theory (Garrett, 2001; Henyey & Pomphrey, 1983). For simplicity, a NIW packet traveling southward and downward from a depth 250 m is considered (i.e., $k = 0$). The dispersion relation of the internal wave is given by

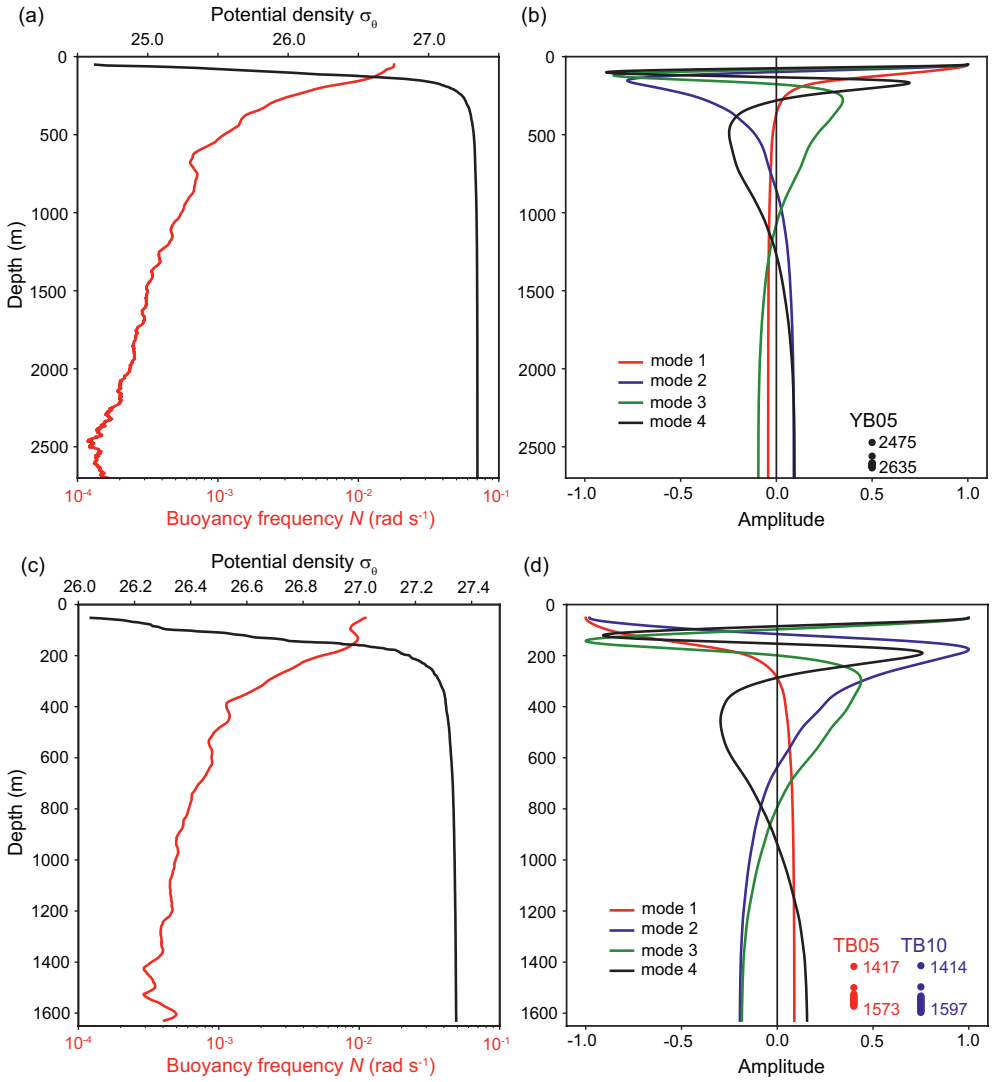

Figure 16. Profiles of potential density (black) and buoyancy frequency N (red) at Stas. YB (a) and TB (c). Right panels show the horizontal flow profiles of the leading four normal modes at Stas. YB (b) and TB (d). The horizontal flow is normalized by the maximum value in each mode. The positions of flow measurement at Sta. YB in May 2014 (YB05, black circles), at Sta. TB in May 2015 (TB05, red circles) and in October 2015 (TB10, blue circles) are also plotted.

$$\omega = F\left(l,m;f\left(y\right),N\left(z\right)\right) = \left(\frac{N\left(z\right)^2 l^2 + f\left(y\right)^2 m^2}{l^2 + m^2}\right)^{1/2} \tag{2}$$

The changes in wavenumber (l, m) and location (y, z) of internal waves are described according to the following four ray equations,

$$\frac{dy}{dt} = \frac{\partial F}{\partial l} = \frac{\left(N^2 - f^2\right)lm^2}{\omega\left(l^2 + m^2\right)^2} \equiv Cg_y \tag{3}$$

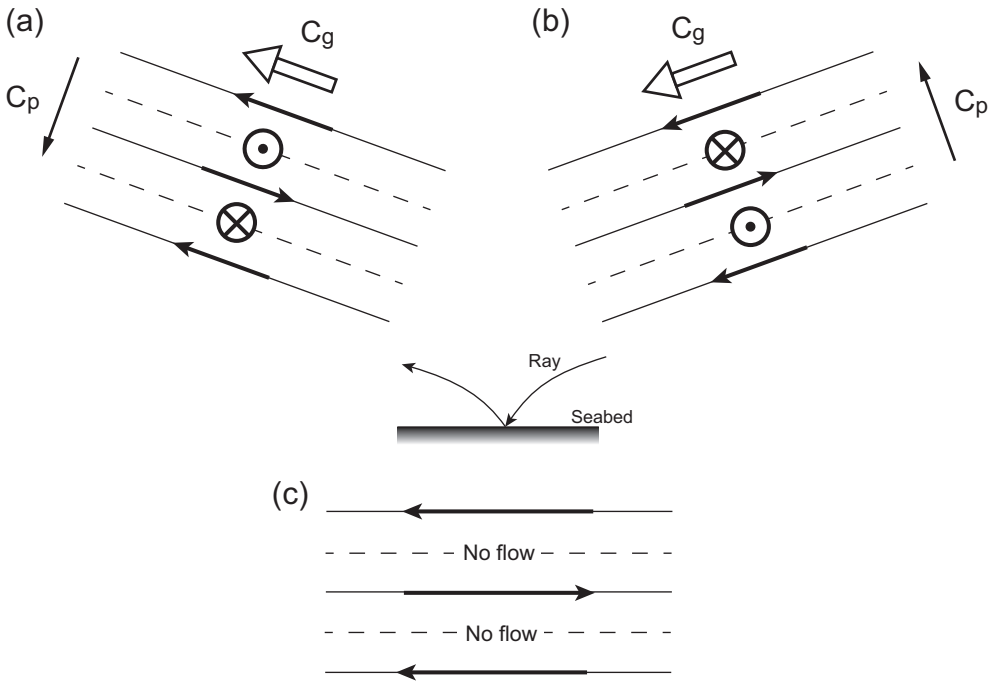

Figure 17. The flow fields in (a) upward-propagating and (b) downward-propagating internal waves. White bold and black thin arrows labeled C_g and C_p denote the group and phase velocities, respectively. The flow field when the downward- and upward-propagating waves were superimposed is shown in (c).

$$\frac{dz}{dt} = \frac{\partial F}{\partial m} - \frac{\left(N^2 - f^2\right) l^2 m}{\omega\left(l^2 + m^2\right)^2} \equiv Cg_z \tag{4}$$

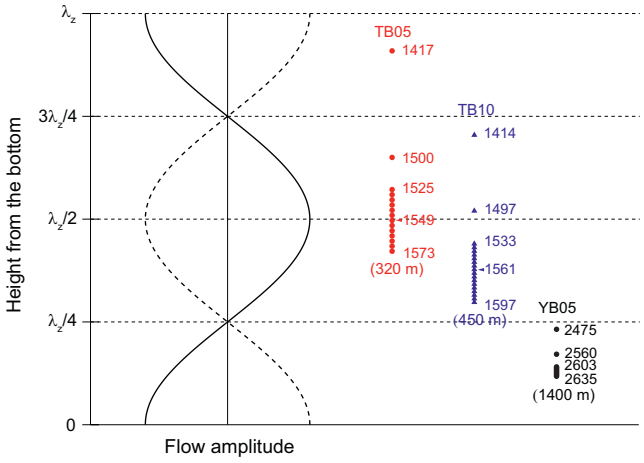

Figure 18. Profile of the horizontal flow amplitude when a downward- and upward-propagating NIWs were superimposed as a function of height from the bottom. The dashed curve indicates the amplitude at opposite phase. The positions of flow measurement at Sta. TB in May 2015 (TB05, red circles), in October 2015 (TB10, blue triangles), and at Sta. YB in May 2014 (YB05, black circles) are also plotted. These positions of flow measurement were scaled by the arbitrarily selected vertical wavelength (numerals in parenthesis) accounting for the observed flow amplitudes (Figure 11).

$$\frac{dl}{dt} = -\frac{\partial F}{\partial y} = -\frac{\beta f}{\omega}\frac{m^2}{l^2 + m^2} = -\frac{\beta f}{\omega}\frac{a^2}{a^2 + 1} \tag{5}$$

$$\frac{dm}{dt} = -\frac{\partial F}{\partial z} = -\frac{N}{\omega}\frac{dN}{dz}\frac{l^2}{l^2 + m^2} = -\frac{N}{\omega}\frac{dN}{dz}\frac{1}{a^2 + 1} \tag{6}$$

where the squared aspect ratio $a^2 = m^2/l^2$. The stratification at Sta. YB is assumed in the entire y–z section (Figure 16a), although significant horizontal density gradients due to the subarctic front exist around 40°N in the real ocean. Initially, the horizontal wavenumber of NIW at 250 m (l_{250}) is specified. The amplitude of vertical wavenumber (m_{250}) is automatically determined by the aspect ratio a at the depth. Since our concern is the southward and downward propagating NIW, l_{250} is taken to be negative, while m_{250} is positive because of the opposite relationship between the vertical phase and group velocities (Figure 17b). The ray of the NIW is traced following Equations 3 4 5 6 at a time step 60 s, assuming $\omega = 0.966 \times 10^{-4}$ rad s^{-1}, $f_0 = f_{YB} = 0.903 \times 10^{-4}$ rad s^{-1}, and $\beta = df/dy = 1.79 \times 10^{-11}$ rad s^{-1} m^{-1}.

First, the ray paths of NIW with $l_{250} = 1.57 \times 10^{-4}$ rad m^{-1} (corresponding to the horizontal wavelength $\lambda_{y250} = 30$ km) started from various latitudes ranging 38.5°N-41.0°N are examined (Figure A2). As the aspect ratio a is a function of not only $N(z)$ but also $f(y)$, the shape of the ray paths is

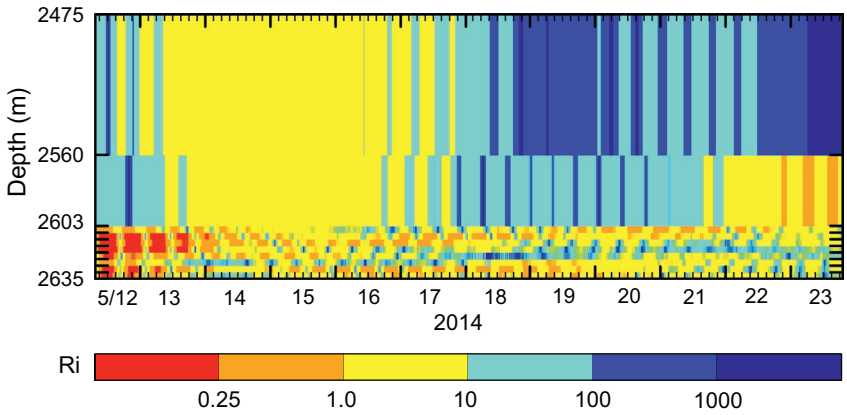

Figure 19. Time-depth diagram of the Richardson number calculated from the vertical shear $S^2 = (\partial u_i/\partial z)^2 + (\partial v_i/\partial z)^2$ at Sta. YB in May 2014 and the profile of N in Figure 16a.

slightly different each other. The results show that the NIWs started from 38.5°N-39.0°N are most plausible waves influencing the deep flow at Sta. YB. Note that this result does not exclude the possibility that these NIWs were excited at further higher latitudes (for example, at the critical latitude 41.5°N). The slope of the ray paths in the upper 250 m layer sharply diminishes due to the strong stratification and the ray paths can be extended to near the critical latitude with considerable variability (Jeon et al., 2019).

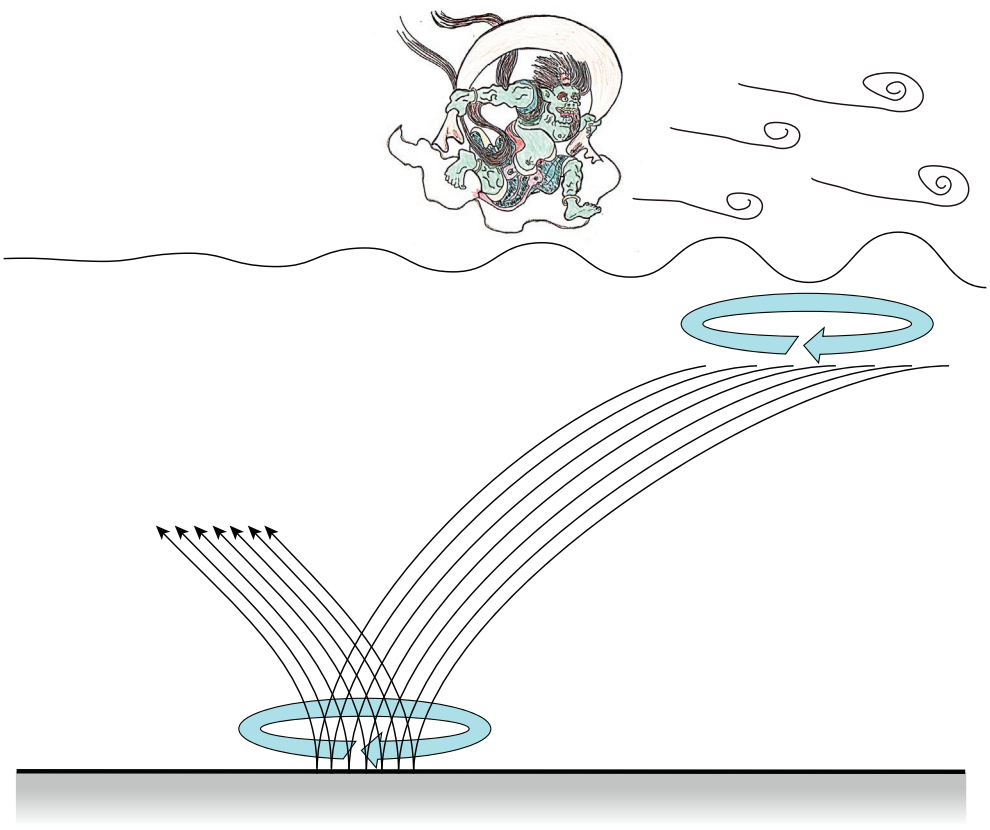

Figure 20. Cartoon of NIWs generated in a wide area by a strong wind event. NIWs propagate along the rainfall-like rays and bounce off the seabed. They interfere to produce intensified near-inertial flows that promote deep mixing.

On the basis of the above results, we next evaluate the horizontal and vertical wavelengths of NIWs at 2,500 m (λ_{y2500} and λ_{z2500}, respectively), which waves were propagated from 250 m at 39°N with various horizontal wavelengths (Table A1). Comparing with the observational results at Sta. YB in May 2014 ($\lambda_{z2500} > 1{,}400$ m, which results in $\lambda_{y2500} > 4$ km), the case $\lambda_{y250} = 5$ km appears to show similar wavelengths at 2,500 m, although this case requires more than 50 days of the traveling time from 250 to 2,500 m. Regarding the vertical group velocity (Cg_z), all the cases exhibit comparable values with the vertical propagation speed of the wave packet (0.75 cm s^{-1}) for the depth range 1,975–2,475 m, while Cg_z for the range 950–1,975 m are one order of magnitude smaller than the corresponding packet propagation speed (1.39 cm s^{-1}). The observed wave packet speed for 1,975–2,475 m is between the cases $\lambda_{y250} = 20$–30 km. The traveling time of these cases is 10–14 days; however, unrealistic vertical wavelengths are estimated at 2,500 m.

Considering uncertainty of the estimate of wave packet speeds and the ray-tracing experiments, 5–30 km of λ_{y250} at 39°N is suggested for the significant NIWs observed at Sta. YB in May 2014. Shcherbina et al. (2003) reported NIW's horizontal wavelength of 38 km in the subarctic front of the Japan Sea. Kawaguchi et al. (2020) also suggested NIW's horizontal wavelength of 30–60 km in the upper 200 m of the Yamato Basin. It should be noted that the horizontal and vertical wavelengths at 250 m differ from those in the surface layer. As the aspect ratio of NIW in the upper 250 m is significantly larger than that below the depth (Figure A1), a longer horizontal wavelength up to several tens kilometers can be expected under the surface mixed layer. In addition, recent studies reported the effective vertical energy transport of NIWs due

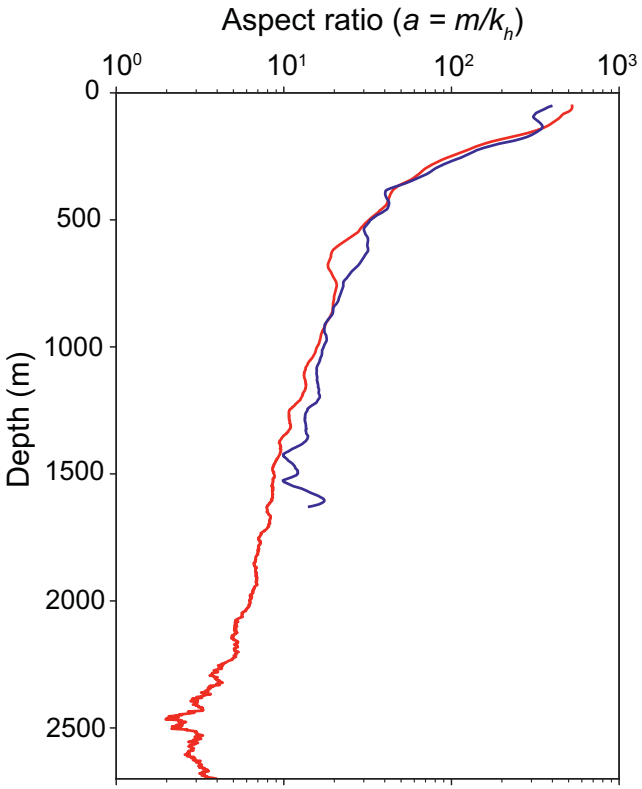

Figure A1. Profiles of the aspect ratio ($a = m/k_h$, k_h denotes horizontal wavenumber) of NIWs at Stas. YB (red) and TB (blue).

to mesoscale eddies with negative vorticity (Jeon et al., 2019; Kawaguchi et al., 2020). This mechanics may explain the discrepancy in the traveling time of NIWs.

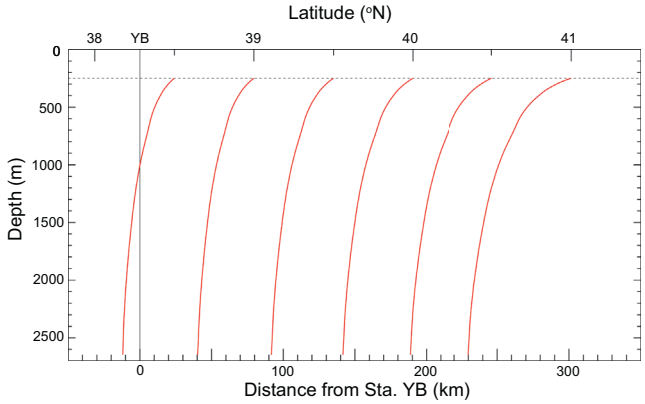

Figure A2. Ray paths of the southward and downward propagating NIW with $\lambda_{y250} = 30$ km (red lines). The tracing of the ray is started from 250 m at every 0.5° in latitude in the range 38.5°N-41.0°N. The vertical thin line denotes the location of Sta. YB and the lower abscissa indicates the distance from Sta. YB. The upper abscissa and horizontal broken line denote the longitude and the positon of 250 m, respectively.

Table A1
Horizontal and Vertical Wavelengths of NIW Emitted From 39°N at 250 m (λ_{y250} and λ_{z250}), Those at 2,500 m (λ_{y2500} and λ_{z2500}), Traveling Time From 250 to 2,500 m ($T_{250-2500}$), and Mean Vertical Group Velocity (Cg_z) for the Depth Ranges 1,975–2,475 and 950–1,975 m

					Cg_z (cm s^{-1})	
λ_{y250} (km)	λ_{z250} (m)	λ_{y2500} (km)	λ_{z2500} (m)	$T_{250-2500}$ (days)	1,975–2,475 m	950–1,975 m
5.0	45	4.7	1,856	57.6	0.16	0.07
10.0	86	9.3	3,566	28.8	0.32	0.15
20.0	179	18.7	7,784	14.4	0.63	0.30
30.0	269	28.1	9,507	9.6	0.93	0.44
40.0	358	37.5	12,569	7.2	1.28	0.59

Acknowledgments
The authors would like to thank the captain and crew of the T/V Nagasaki Maru and T. Mada for helping with the field observations. T. Matsuno and colleagues in the Regional Oceanography Section, RIAM, Kyushu University are also acknowledged for useful discussions. The original manuscript has been greatly improved by insightful comments from three anonymous reviewers. This work was supported by JSPS KAKENHI, Grant Numbers JP26610151 and JP18H03741, and the Environment Research and Technology Development Fund of the Ministry of the Environment, Japan (2-1604). H. R. Shin was supported in part by the Collaborative Research Program of the Research Institute for Applied Mechanics, Kyushu University (18EA-6).

Data Availability Statement

The authors have deposited their data sets on a general repository Zenodo as http://doi.org/10.5281/zenodo.3959947. The GPV/MSM data used in this study were NetCDF files provided from Research Institute for Sustainable Humanosphere, Kyoto University (http://database.rish.kyoto-u.ac.jp/arch/jmadata/gpv-netcdf.html). Other data sets used in this study can be download from the relevant open access websites described in the manuscript.

References

Alford, M. H. (2001). Internal swell generation: The spatial distribution of energy flux from the wind to mixed layer near-inertial motions. *Journal of Physical Oceanography*, *31*(8), 2359–2368. https://doi.org/10.1175/1520-0485(2001)031%3C2359:ISGTSD%3E2.0.CO;2

Alford, M. H. (2003a). Redistribution of energy available for ocean mixing by long-range propagation of internal waves. *Nature*, *423*(6936), 159–162. https://www.nature.com/articles/nature01628

Alford, M. H. (2003b). Improved global maps and 54-year history of wind-work on ocean inertial motions. *Geophysical Research Letters*, *30*(8), 1424–1427. https://doi.org/10.1029/2002GL016614

Alford, M. H. (2010). Sustained, full-water-column observations of internal waves and mixing near Mendocino escarpment. *Journal of Physical Oceanography*, *40*(12), 2643–2660. https://doi.org/10.1175/2010JPO4502.1

Alford, M. H., Cronin, M. F., & Klymak, J. M. (2012). Annual cycle and depth penetration of wind-generated near-inertial internal waves at ocean station Papa in the northeast Pacific. *Journal of Physical Oceanography*, *42*(6), 889–909. https://doi.org/10.1175/JPO-D-11-092.1

Alford, M. H., & Gregg, M. C. (2001). Near-inertial mixing: Modulation of shear, strain and microstructure at low latitude. *Journal of Geophysical Research*, *106*(C8), 16947–16968. https://doi.org/10.1029/2000JC000370

Alford, M. H., MacKinnon, J. A., Pinkel, R., & Klymak, J. M. (2017). Space–time scales of shear in the North Pacific. *Journal of Physical Oceanography*, *47*(10), 2455–2478. https://doi.org/10.1175/JPO-D-17-0087.1

Alford, M. H., MacKinnon, J. A., Simmons, H. L., & Nash, J. D. (2016). Near-inertial internal gravity waves in the ocean. *Annual Review of Marine Science*, *8*, 95–123. https://doi.org/10.1146/annurev-marine-010814-015746

Alford, M. H., & Whitmont, M. (2007). Seasonal and spatial variability of near-inertial kinetic energy from historical mooed velocity records. *Journal of Physical Oceanography*, *37*(8), 2022–2037. https://doi.org/10.1175/JPO3106.1

Cushman-Roisin, B., & Beckers, J. M. (2011). *Introduction to geophysical fluid dynamics: Physical and numerical aspects* (2nd ed.). Massachusetts, MA: Academic Press.

D'Asaro, E. A. (1985). The energy flux from the wind to near-inertial motions in the surface mixed layer. *Journal of Physical Oceanography*, *15*(8), 1043–1059. https://doi.org/10.1175/1520-0485(1985)015%3C1043:TEFFTW%3E2.0.CO;2

Eriksen, C. C. (1982). Observations of internal wave reflection off sloping bottoms. *Journal of Geophysical Research*, *87*(C1), 525–538. https://doi.org/10.1029/JC087iC01p00525

Furuichi, N., Hibiya, T., & Niwa, Y. (2008). Model-predicted distribution of wind-induced internal wave energy in the world's oceans. *Journal of Geophysical Research*, *113*(C9), C09034. https://doi.org/10.1029/2008JC004768

Gamo, T., & Horibe, Y. (1983). Abyssal circulation in the Japan Sea. *Journal of the Oceanographical Society of Japan*, *39*(5), 220–230. https://link.springer.com/article/10.1007/BF02070392

Gamo, T., Nozaki, Y., Sakai, H., Nakai, T., & Tsubota, H. (1986). Spacial and temporal variations of water characteristics in the Japan Sea bottom layer. *Journal of Marine Research*, *44*(4), 781–793. https://doi.org/10.1357/002224086788401620

Garrett, C. (2001). What is the "near-inertial" band and why is it different from the rest of the internal wave spectrum? *Journal of Physical Oceanography*, *31*(4), 962–971. https://doi.org/10.1175/1520-0485(2001)031%3C0962:WITNIB%3E2.0.CO;2

Gill, A. E. (1982). *Atmosphere-ocean dynamics*. Orlando: Academic Press.

Henyey, F. S., & Pomphrey, N. (1983). Eikonal description of internal wave interactions: A non-diffusive picture of "induced diffusion". *Dynamics of Atmospheres and Oceans*, *7*(4), 189–219. https://doi.org/10.1016/0377-0265(83)90005-2

Hogan, P. J., & Hurlburt, H. E. (2000). Impact of upper ocean-topographical coupling and isopycnal outcropping in Japan/East Sea models with 1/8° to 1/64° resolution. *Journal of Physical Oceanography*, *30*(10), 2535–2561. https://doi.org/10.1175/1520-0485(2000)030%3C2535:IOUOTC%3E2.0.CO;2

Ito, H., & Minobe, S. (2010). Data analysis method in meteorology and physical oceanography (Meteorological Research Note, Vol. 221). Tokyo: Meteorological Society of Japan.

Japan Meteorological Agency (2013). http://www.data.jma.go.jp/gmd/kaiyou/db/vessel_obs/data-report/html/ship/cruisedata.php?id=KS1308

Japan Meteorological Agency (2014). http://www.data.jma.go.jp/gmd/kaiyou/db/vessel_obs/data-report/html/ship/cruisedata.php?id=KS1406

Jeon, C., Park, J.-H., & Park, Y.-G. (2019). Temporal and spatial variability of near-inertial waves in the East/Japan Sea from a high-resolution wind-forced ocean model. *Journal of Geophysical Research: Oceans*, *124*(8), 6015–6029. https://doi.org/10.1029/2018JC014802

Jordi, A., & Wang, D. P. (2008). Near-inertial motions in and around the Palamós submarine canyon (NW Mediterranean) generated by a severe storm. *Continental Shelf Research*, *28*(17), 2523–2534. https://doi.org/10.1016/j.csr.2008.07.008

Kawaguchi, Y., Wagawa, T., & Igeta, Y. (2020). Near-inertial internal waves and multiple-inertial oscillations trapped by negative vorticity anomaly in the central Sea of Japan. *Progress in Oceanography*, *181*, 102240. https://doi.org/10.1016/j.pocean.2019.102240

Kim, Y.-J. (2007). *A study on the Japan/East Sea oceanic circulation using an extra fine resolution model* (Doctoral dissertation). Fukuoka: Kyushu University.

Kunze, E. (1985). Near-inertial wave propagation in geostrophic shear. *Journal of Physical Oceanography*, *15*(5), 544–565. https://doi.org/10.1175/1520-0485(1985)015%3C0544:NIWPIG%3E2.0.CO;2

Large, W. G., & Pond, S. (1981). Open ocean momentum flux measurements in moderate to strong winds. *Journal of Physical Oceanography*, *11*(3), 324–336. https://doi.org/10.1175/1520-0485(1981)011%3C0324:OOMFMI%3E2.0.CO;2

Lien, R.-C., Sanford, T. B., Jan, S., Chang, M.-H., & Ma, B. B. (2013). Internal tides on the East China Sea continental slope. *Journal of Marine Research*, *71*(1–2), 151–186. https://doi.org/10.1357/002224013807343461

Matsuno, T., Endoh, T., Hibiya, T., Senjyu, T., & Watanabe, M. (2015). Formation of the well-mixed homogeneous layer in the bottom water of the Japan Sea. *Journal of Oceanography*, *71*(4), 441–447. https://doi.org/10.1007/s10872-015-0303-7

Melet, A., Hallberg, R., Legg, S., & Polzin, K. (2013). Sensitivity of the ocean state to the vertical distribution of internal-tide-driven mixing. *Journal of Physical Oceanography*, *43*(3), 602–615. https://doi.org/10.1175/JPO-D-12-055.1

Mori, K., Matsuno, T., & Senjyu, T. (2005). Seasonal/spatial variations of the near-inertial oscillations in the deep water of the Japan Sea. *Journal of Oceanography*, *61*(4), 761–773. https://doi.org/10.1007/s10872-005-0082-7

Munk, W., & Wunsch, C. (1998). Abyssal recipes II: Energetic of tidal and wind mixing. *Deep-Sea Research I: Oceanographic Research Papers*, *45*(12), 1977–2010. https://doi.org/10.1016/S0967-0637(98)00070-3

Nikurashin, M., & Ferrari, R. (2010a). Radiation and dissipation of internal waves generated by geostrophic motions impinging on small-scale topography: Application to the Southern Ocean. *Journal of Physical Oceanography*, *40*(9), 2025–2042. https://doi.org/10.1175/2010JPO4315.1

Nikurashin, M., & Ferrari, R. (2010b). Radiation and dissipation of internal waves generated by geostrophic motions impinging on small-scale topography: Theory. *Journal of Physical Oceanography*, *40*(5), 1055–1074. https://doi.org/10.1175/2009JPO4199.1

Niwa, Y., & Hibiya, T. (2001). Numerical study of the spatial distribution of the M_2 internal tide in the Pacific Ocean. *Journal of Geophysical Research*, *106*(C10), 22414–22449. https://doi.org/10.1029/2000JC000770

Oey, L.-Y., Inoue, M., Lai, R., Lin, X.-H., Welsh, S. E., & Rouse, L. J., Jr. (2008). Stalling of near-inertial waves in a cyclone. *Geophysical Research Letters*, *35*(12), L12604. https://doi.org/10.1029/2008GL034273

Park, J.-H., & Watts, D. R. (2005). Near-inertial oscillations interacting with mesoscale circulation in the southwestern Japan/East Sea. *Geophysical Research Letters*, *32*(10), L10611. https://doi.org/10.1029/2005GL022936

Park, J.-H., & Watts, D. R. (2006). Internal tides in the southwestern Japan/East Sea. *Journal of Physical Oceanography*, *36*(1), 22–34. https://doi.org/10.1175/JPO2846.1

Park, Y.-G., Park, J.-H., Lee, H. J., Min, H. S., & Kim, S.-D. (2013). The effects of geothermal heating on the East/Japan Sea circulation. *Journal of Geophysical Research: Oceans*, *118*(4), 1893–1905. https://doi.org/10.1002/jgrc.20161

Phillips, O. M. (1977). *The dynamics of the upper ocean* (2nd ed.). Cambridge: Cambridge University Press.

Pollard, R. T., & Millard, R. C., Jr. (1970). Comparison between observed and simulated wind-generated inertial oscillations. *Deep Sea Research and Oceanographic Abstracts*, *17*(4), 813–821. https://doi.org/10.1016/0011-7471(70)90043-4

Polzin, K. L., Toole, J. M., Ledwell, J. R., & Schmitt, R. W. (1997). Spatial variability of turbulent mixing in the abyssal ocean. *Science*, *276*(5309), 93–96. https://doi.org/10.1126/science.276.5309.93

Puig, P., Palanques, A., Guillén, J., & García-Ladona, E. (2000). Deep slope currents and suspended particle fluxes in and around the Foix submarine canyon (NW Mediterranean). *Deep Sea Research Part I: Oceanographic Research Papers*, *47*(3), 343–366. https://doi.org/10.1016/S0967-0637(99)00062-X

Samelson, R. M. (1998). Large-scale circulation with locally enhanced vertical mixing. *Journal of Physical Oceanography*, *28*(4), 712–726. https://doi.org/10.1175/1520-0485(1998)028%3C0712:LSCWLE%3E2.0.CO;2

Sarkar, S., & Scotti, A. (2017). From topographic internal gravity waves to turbulence. *Annual Review of Fluid Mechanics*, *49*, 195–220. https://doi.org/10.1146/annurev-fluid-010816-060013

Senjyu, T. (2015). Observation of near-inertial internal waves in the abyssal Japan Sea. *La Mer*, *53*, 43–51. http://www.sfjo-lamer.org/la_mer/53-3_4/53-3-4-1.pdf

Senjyu, T. (2020). Long-term changes in the abyssal Japan Sea (East Sea): A physical view. In C. T. A. Chen & X. Guo (Eds.), *Changing Asia-Pacific Marginal Seas, Atmosphere, Earth, Ocean & Space* (pp. 69–85). Singapore: Springer Nature. Retrieved from https://doi.org/10.1007/978-981-15-4886-4_5

Senjyu, T., Aramaki, T., Otosaka, S., Togawa, O., Danchenkov, M., Karasev, E., & Volkov, Y. (2002). Renewal of the bottom water after the winter 2000–2001 may spin-up the thermohaline circulation in the Japan Sea. *Geophysical Research Letters*, *29*(7), 53-1–53-3. https://doi.org/10.1029/2001GL014093

Senjyu, T., Isoda, Y., Aramaki, T., Otosaka, S., Fujio, S., Yanagimoto, D., et al. (2005a). Benthic front and the Yamato Basin Bottom Water in the Japan Sea. *Journal of Oceanography*, *61*(6), 1047–1058. https://doi.org/10.1007/s10872-006-0021-2

Senjyu, T., Shin, H.-R., Yoon, J.-H., Nagano, Z., An, H.-S., Byun, S.-K., & Lee, C.-K. (2005b). Deep flow field in the Japan/East Sea as deduced from direct current measurements. *Deep Sea Research Part II: Topical Studies in Oceanography*, *52*(11–13), 1726–1741. https://doi.org/10.1016/j.dsr2.2003.10.013

Senjyu, T., & Sudo, H. (1993). Water characteristics and circulation of the upper portion of the Japan Sea Proper Water. *Journal of Marine Systems*, *4*(4), 349–362. https://doi.org/10.1016/0924-7963(93)90029-L

Senjyu, T., & Sudo, H. (1994). The upper portion of the Japan Sea Proper Water; its source and circulation as deduced from isopycnal analysis. *Journal of Oceanography*, *50*(6), 663–690. https://doi.org/10.1007/BF02270499

Shcherbina, A. Y., Talley, L. D., Firing, E., & Hacker, P. (2003). Near-surface frontal zone trapping and deep upward propagation of internal wave energy in the Japan/East Sea. *Journal of Physical Oceanography*, *33*(4), 900–912. https://doi.org/10.1175/1520-0485(2003)33%3C900:NFZTAD%3E2.0.CO;2

Silverthorne, K. E., & Toole, J. M. (2009). Seasonal kinetic energy variability of near-inertial motions. *Journal of Physical Oceanography*, *39*(4), 1035–1049. https://doi.org/10.1175/2008JPO3920.1

Takematsu, M., Nagano, Z., Ostrovskii, A. G., Kim, K., & Volkov, Y. (1999). Direct measurements of deep currents in the northern Japan Sea. *Journal of Oceanography*, *55*(2), 207–216. https://doi.org/10.1023/A:1007842013257

Tool, J. M. (2007). Temporal characteristics of abyssal finescale motions above rough bathymetry. *Journal of Physical Oceanography*, *37*(3), 409–427. https://doi.org/10.1175/JPO2988.1

van der Lee, E. M., & Umlauf, L. (2011). Internal wave mixing in the Baltic Sea: Near-inertial waves in the absence of tides. *Journal of Geophysical Research*, *116*(C10). https://doi.org/10.1029/2011JC007072

Watanabe, M., & Hibiya, T. (2002). Global estimates of the wind-induced energy flux to inertial motions in the surface mixed layer. *Geophysical Research Letters*, *29*(8), 1239. https://doi.org/10.1029/2001GL014422

Watanabe, M., & Hibiya, T. (2018). A near-inertial current event in the homogeneous deep layer of the northern Sea of Japan during winter. *Journal of Oceanography*, *74*(2), 209–218. https://doi.org/10.1007/s10872-017-0451-z

Worthington, L. V. (1980). The water masses of the world ocean: Some results of a fine-scale census. In B. A. Warren & C. Wunsch (Eds.), *Evolution of physical oceanography* (pp. 42–69). Cambridge: MIT Press.

Yasui, M., Yasuoka, T., Tanioka, K., & Shiota, O. (1967). Oceanographic studies of the Japan Sea (1) – Water characteristics. *The Oceanographical Magazine*, *19*, 177–192.